

THE GRISM LENS-AMPLIFIED SURVEY FROM SPACE (GLASS). VI. COMPARING THE MASS AND LIGHT IN MACSJ0416.1-2403 USING FRONTIER FIELD IMAGING AND GLASS SPECTROSCOPY

A. HOAG¹, K. HUANG¹, T. TREU², M. BRADAČ¹, K. B. SCHMIDT³, X. WANG^{2,4}, G. B. BRAMMER⁵, A. BROUSSARD⁶,
R. AMORIN⁷, M. CASTELLANO⁷, A. FONTANA⁷, E. MERLIN⁷, T. SCHRABBACK⁸, M. TRENTI⁹, B. VULCANI^{9,10}

¹ Department of Physics, University of California, Davis, CA, 95616, USA

² Department of Physics and Astronomy, UCLA, Los Angeles, CA, 90095-1547, USA

³ Leibniz-Institut für Astrophysik Potsdam (AIP), An der Sternwarte 16, 14482 Potsdam, Germany

⁴ Department of Physics, University of California, Santa Barbara, CA, 93106-9530, USA

⁵ Space Telescope Science Institute, 3700 San Martin Drive, Baltimore, MD, 21218, USA

⁶ Department of Physics and Astronomy, Texas A&M, College Station, TX 77843, USA

⁷ INAF - Osservatorio Astronomico di Roma Via Frascati 33 - 00040 Monte Porzio Catone, 00040 Rome, Italy

⁸ Argelander-Institut für Astronomie, Auf dem Hügel 71, D-53121 Bonn, Germany

⁹ School of Physics, University of Melbourne, Parkville, Victoria, Australia and

¹⁰ Kavli Institute for the Physics and Mathematics of the Universe (WPI), Todai Institutes for Advanced Study, the University of Tokyo, Kashiwa, 277-8582, Japan

Draft version March 3, 2016

ABSTRACT

We present a strong and weak gravitational lens model of the galaxy cluster MACSJ0416.1-2403, constrained using spectroscopy from the *Grism Lens-Amplified Survey from Space* (GLASS) and *Hubble Frontier Fields* (HFF) imaging data. We search for emission lines in known multiply imaged sources in the GLASS spectra, obtaining secure spectroscopic redshifts of 31 multiple images belonging to 16 distinct source galaxies. The GLASS spectra provide the first spectroscopic measurements for 6 of the source galaxies. The weak lensing signal is acquired from 884 galaxies in the F606W HFF image. By combining the weak lensing constraints with 15 multiple image systems with spectroscopic redshifts and 9 multiple image systems with photometric redshifts, we reconstruct the gravitational potential of the cluster on an adaptive grid. The resulting total mass density map is compared with a stellar mass density map obtained from the deep *Spitzer* Frontier Fields imaging data to study the relative distribution of stellar and total mass in the cluster. We find that the projected stellar mass to total mass ratio, f_* , varies considerably with the stellar surface mass density. The mean projected stellar mass to total mass ratio is $\langle f_* \rangle = 0.009 \pm 0.003$ (stat.), but with a systematic error as large as 0.004 – 0.005, dominated by the choice of the IMF. We find agreement with several recent measurements of f_* in massive cluster environments. The lensing maps of convergence, shear, and magnification are made available to the broader community in the standard HFF format.

Subject headings: galaxies: clusters: individual (MACS J0416.1-2403)

1. INTRODUCTION

Gravitational lensing by clusters of galaxies is now a commonplace tool in astrophysics and cosmology (see Treu & Ellis 2014 for a recent review). The magnification of background objects produced by cluster lenses has been used to find extremely distant and faint galaxies (e.g. Zheng et al. 2012; Coe et al. 2013; Zitrin et al. 2014). As a result, clusters of galaxies are becoming increasingly popular tools for studying the epoch of reionization. Cluster-scale lensing has also been used to determine the spatial distribution of the total cluster mass, revealing insights into physics of dark matter and structure formation (e.g. Clowe et al. 2006; Bradač et al. 2006; Sand et al. 2008; Newman et al. 2013; Sharon et al. 2014; Merten et al. 2015).

The Hubble Frontier Fields (HFF) program (PI Lotz; Lotz et al. in prep.) is imaging six clusters of galaxies and six parallel fields to extreme depths in seven optical and near-infrared (NIR) bands, using the Advanced Camera for Surveys (ACS) and the Wide Field Camera 3 (WFC3). A principal objective of the HFF initiative is to search for magnified objects behind the six clusters. Lens models providing accurate magnification maps are needed to determine the unlensed (intrinsic) properties of

the background objects. Lens models are primarily constrained by multiply imaged galaxies and weakly sheared sources. The added depth of the HFF images allows one to identify more multiply imaged galaxies, thus increasing the number of constraints and therefore the quality of the lens models. The CLASH¹ images (limiting magnitude ~ 27 AB mag for a 5σ point source Postman et al. 2012) revealed ~ 10 candidate multiple image systems per cluster (e.g. Zitrin et al. 2015). The release of the HFF images (limiting magnitude ~ 29 AB mag for a 5σ point source) has approximately tripled the number of known multiply imaged galaxies for the four clusters analyzed so far (e.g. Jauzac et al. 2015a, 2014; Diego et al. 2015b; Wang et al. 2015; Treu et al. 2016).

While the added depth of the HFF imaging has enabled the photometric identification of a greater number of multiply imaged systems, the redshifts of the new systems remain uncertain without spectroscopic follow up. The redshifts must be well-constrained in order to be useful for the lens models. It has recently been shown that the number of *spectroscopic* systems has a strong influence on the quality of the lens model (Rodney et al.

¹ The Cluster Lensing And Supernova Survey with Hubble (CLASH); <http://www.stsci.edu/~postman/CLASH/Home.html>

2015a,b). Photometric redshifts are useful when spectroscopy is lacking, but they can be prone to catastrophic errors, especially for sources at or near the limiting magnitude of the image. An alternative approach to photometric redshifts is to estimate the redshift of new multiply imaged systems using an existing model (e.g. Jauzac et al. 2014). This method can potentially introduce confirmation bias in the modeling process. That is, unless a correct lens model has already been obtained, the predicted redshifts of the multiply imaged galaxies may be incorrect, and the uncertainties may be underestimated. Unless decided upon in advance, different approaches to determining redshifts in the absence of spectroscopic data can lead to different constraints among teams modeling the same cluster.

It is therefore paramount to obtain spectroscopic redshifts for the multiply imaged systems in the HFF. The Grism Lens-Amplified Survey from Space (GLASS) data for MACSJ0416.1-2403 (MACSJ0416 hereafter) is one such effort. GLASS^{2,3} is a large *HST* program that has obtained deep NIR grism spectroscopy in the fields of ten clusters, including all six HFF clusters. For details on the observation strategy and data products of GLASS, see Schmidt et al. (2014) and Treu et al. (2015).

In this paper, we present new spectroscopic redshifts from GLASS and combine them with redshifts from the literature to model the HFF images of MACSJ0416. When spectroscopy is not available, we use photometric redshifts tested against GLASS spectra of singly-imaged objects. The paper is organized as follows. In Section 2 we give an overview of the optical and NIR HFF and mid-IR *Spitzer* Frontier Fields imaging data, as well as the GLASS NIR spectroscopic data. In Section 3 we briefly cover the reduction and analysis of the GLASS data. In Section 4 we describe the process of selecting the set of multiple images used to constrain the lens model and discuss the GLASS spectroscopic measurements. In Section 5 we present our lens model and compare it to other lens models of the cluster using similar constraints. In Section 6, we study the relative distribution of stellar and total mass. Finally, we summarize our results in Section 7. We adopt a standard concordance cosmology with $\Omega_m = 0.3$, $\Omega_\Lambda = 0.7$ and $h = 0.7$. All magnitudes are given in the AB system (Oke 1974).

2. DATA

Discovered by the MACS survey (Ebeling et al. 2001) as a result of its large X-ray luminosity ($\sim 10^{46}$ erg s^{-1} ; Mann & Ebeling 2012), MACSJ0416 was found to likely be a binary head-on merging cluster system. The first optical and NIR *HST* imaging data of MACSJ0416 were obtained by the CLASH survey. The ESO VIMOS large program CLASH-VLT (186.A-0798; PI: P. Rosati), a spectroscopic campaign designed to obtain thousands of optical spectra in the CLASH cluster fields with VIMOS on the Very Large Telescope (VLT), recently found further evidence for the merging state of the cluster (Balestra et al. 2015).

Here, we present lens modeling and spectroscopy results using the deepest optical and NIR imaging and spectroscopy data newly acquired with *Hubble*, as part of

the HFF initiative (2.1) and the GLASS program (3), following our study of Abell 2744 in Wang et al. (2015). We also use mid-IR imaging data acquired with the *Spitzer* Space Telescope (2.2; Werner et al. 2004) obtained by the DDT program #90258 (Capak et al. in prep).

2.1. Hubble Frontier Fields Imaging

Ultra deep *HST* images of six clusters (Abell 370, Abell 2744, MACSJ2129, MACSJ0416, MACSJ0717, and MACSJ1149) are being obtained as part of the HFF⁴. The 5σ point source limiting magnitudes are roughly 29 ABmag in both the ACS/optical (F435W, F606W, F814W) and WFC3/IR filters (F105W, F125W, F140W, F160W). Observations of MACSJ0416 were completed in September, 2014.

2.2. Spitzer Frontier Fields

As a part of the HFF campaign, deep *Spitzer*/IRAC images in channels 1 and 2 (at $3.6 \mu m$ and $4.5 \mu m$, respectively) were taken through the *Spitzer* Frontier Fields program⁵. In this work, we use the full-depth *Spitzer*/IRAC mosaics for MACSJ0416 released by Capak et al. (in prep). The IRAC mosaics reach ~ 50 hr depth per channel in the HFF *primary* field and the *parallel* field ($\sim 6'$ to the west of the primary field). Due to *Spitzer* roll angle constraints and low-background requirements, six additional *flanking* fields exist around the HFF primary and parallel fields with uneven coverage in channels 1 and 2. The exposures were drizzled onto a $0''.6 \text{ pix}^{-1}$ grid, and within the *HST* primary field footprint there are ~ 1800 frames (with *FRAMETIME* ~ 100 s) per output pixel. In the primary and parallel fields, the nominal 5σ depth of a point source reaches 26.6 mag at $3.6 \mu m$ and 26.0 mag at $4.5 \mu m$. However, this sensitivity might not be reached near the cluster center due to blending with cluster members and the diffuse intra-cluster light (ICL).

3. GLASS OBSERVATION AND DATA REDUCTION

GLASS (GO-13459; PI: Treu; Schmidt et al. 2014; Treu et al. 2015) observed 10 massive galaxy clusters with the *HST* WFC3-IR G102 and G141 grisms between December 2013 and January 2015. Each of the clusters targeted by GLASS has deep multi-band *HST* imaging from the HFF (2.1) and/or from CLASH. Each cluster is observed at two position angles (P.A.s) approximately 90 degrees apart to facilitate deblending and extraction of the spectra. Short exposures are taken through filters F105W or F140W during every visit to help calibrate the spectra, model the background, model the contaminating objects, and identify supernovae by difference imaging. The total exposure time per cluster is 14 orbits, distributed as to provide approximately uniform sensitivity across the entire wavelength coverage $0.8 \mu m$ to $1.7 \mu m$. Parallel observations are taken with the ACS F814W direct image and G800L grism to map the cluster infall regions. Here we focus on the NIR data on the MACSJ0416 cluster core.

The two P.A.s of GLASS data analyzed here were taken on November 23 and 30, 2014 (P.A. = 164°) and January 13 and 18, 2015 (P.A. = 247°), respectively. The

² <http://glass.astro.ucla.edu>

³ <https://archive.stsci.edu/prepds/glass/>

⁴ <http://www.stsci.edu/hst/campaigns/frontier-fields>

⁵ <http://ssc.spitzer.caltech.edu/warmmission/scheduling/approvedprograms/ddt/frontier/>

TABLE 1
GLASS GRISM AND IMAGING
EXPOSURE TIMES FOR
MACSJ0416

Filter	P.A./ (deg.)	$t_{\text{exp.}}/(\text{s})$
G102	164	10929
G102	247	10929
G141	164	4312
G141	247	4312
F105W	164	1068
F105W	247	1068
F140W	164	1573
F140W	247	1423

NOTE. — Exposure times are for the cluster core of MACSJ0416 only.

resulting total exposure times for the individual grism observations are shown in Table 1. Prior to reducing the complete GLASS data, He Earth-glow is removed from individual exposures (Brammer et al. 2014).

The GLASS observations are designed to follow the 3D-HST observing strategy (Brammer et al. 2012) and were processed with an updated version of the 3D-HST reduction pipeline⁶ (Momcheva et al. 2015). Below we summarize the main steps in the reduction process of the GLASS data but refer to Brammer et al. (2012) and Momcheva et al. (2015) and the GLASS survey paper (Treu et al. 2015) for further details. The GLASS data were taken in a 4-point dither pattern identical to the one shown in Figure 3 of Brammer et al. (2012) to reduce susceptibility to bad pixels and cosmic rays and to improve sub-pixel sampling of the WFC3 point spread function. At each dither position, a direct and a grism exposure were taken. The direct images are commonly taken in the filter with passband overlapping in wavelength with the grism, i.e., F105W for G102 and F140W for G141. However, to accommodate searches for supernovae and the characterization of their light curves in GLASS clusters, each individual visit is designed to have imaging in both filters. Hence several pairs of F140W+G102 observations exist in the GLASS data. This does not affect the reduction or the extraction of the individual GLASS spectra.

The individual exposures were combined into mosaics using AstroDrizzle from the DrizzlePac software package (Gonzaga 2012). All direct image exposures were aligned using *tweakreg*, with background subtracted from the exposures by fitting a second order polynomial to each of the source-subtracted exposures. We subtracted the background of the grism exposures using the master sky images and algorithm presented by Brammer et al. (2015). The individual sky-subtracted exposures were combined using a pixel scale of $0''.06$ per pixel (\sim half a native WFC3 pixel). In Figure 1 we show a color composite image of MACSJ0416, using the optical and NIR coadded imaging from HFF and CLASH combined with the NIR imaging from GLASS. The green (red) square shows the GLASS footprint for P.A. = 164° (P.A. = 247°). The fiducial cluster redshift used by the HFF lens modeling team and adopted throughout the paper is $z_{\text{cluster}} = 0.396$. The two brightest cluster galaxies

(BCGs) (NE and SW) are labeled in the figure. The NE BCG and the SW BCG are at redshifts $z = 0.395$ and $z = 0.400$, respectively (Balestra et al. 2015). Figure 2 shows the full field-of-view mosaics of the two NIR grisms (G102 on the left and G141 on the right) at the two GLASS position angles for MACSJ0416. The contamination model was computed and one- and two-dimensional spectra were extracted from 2×2 “interlaced” versions of the grism mosaics following the procedure outlined in detail by Momcheva et al. (2015), where the source positions and extent were determined with the *SExtractor* (Bertin & Arnouts 1996) software run on the corresponding direct image mosaics.

4. IDENTIFICATION OF MULTIPLE IMAGES

In this section we describe how we identify and vet multiple image candidates using the HFF imaging (4.1) and GLASS spectroscopic (4.2 and 4.3) data.

4.1. Imaging data: identification and photometric redshifts

Zitrin et al. (2013) published the first detailed strong lensing analysis of MACSJ0416. They identified over 70 multiple images (23 source galaxies) in the CLASH imaging data, making MACSJ0416 the most prolific CLASH cluster in terms of multiply imaged galaxies (Zitrin et al. 2015). With the addition of the much deeper HFF data, 272 multiple images (92 source galaxies) have been identified in MACSJ0416 (Jauzac et al. 2014; Diego et al. 2015a; Kawamata et al. 2015). We list all of the multiple images in Table 2 and show their positions behind the cluster in Figure 3.

Several efforts have been made to spectroscopically confirm the redshifts of the strongly-lensed galaxy candidates in MACSJ0416 (Zitrin et al. 2013; Jauzac et al. 2014; Richard et al. 2014; Johnson et al. 2014; Grillo et al. 2015; Balestra et al. 2015, Rodney et al. in prep.). Images belonging to systems 1, 2, 3, 4, 5, 7, 10, 13, 14, 16, 17, 23, 26, and 28 have been targeted by multiple authors, leading to agreement in the spectroscopic redshift within the uncertainties, with the exception of system 14. This system will be discussed in more detail in Section 4.2. When spectroscopy is lacking, confirming that images belong to the same source is more difficult. Inspired by a previous collaborative effort to model the HFF clusters as well as the recent rigorous vetting procedure developed by Wang et al. (2015), a new collaborative effort was undertaken by seven teams simultaneously modeling the HFF galaxy clusters to assign quality grades to the multiple image candidates. The grading was done independently by each of the seven teams and focused on ensuring consistency of the morphologies and colors of multiple images of the same source galaxy. Each team assigned each multiple image candidate a grade on a scale from 1-4, where 1 meant secure and 4 meant untrustworthy. The results from the grading process were divided into the categories: “Gold,” “Silver,” and “Bronze.” The Gold category was reserved for spectroscopically confirmed multiple images that also received an average grade of < 1.5 . The multiple images confirmed using GLASS spectroscopy that are presented in this work were included in the Gold sample. The Silver category corresponded to images lacking spectra but receiving a unanimous vote of 1. Bronze was assigned to

⁶ <http://code.google.com/p/threedhst/>

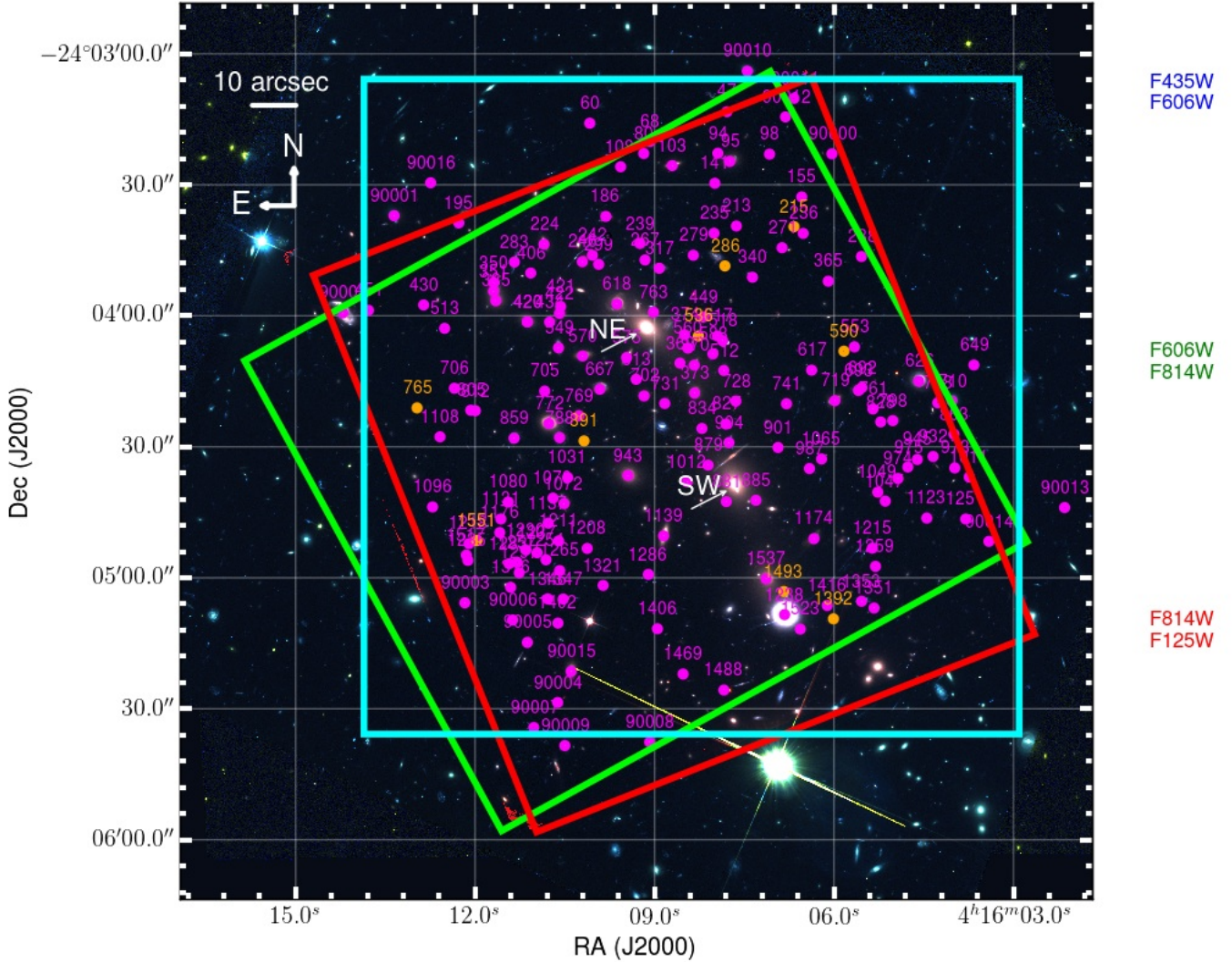


FIG. 1.— Color composite image of MACSJ0416 based on HFF (Lotz et al. in prep.), CLASH (Postman et al. 2012) and GLASS (Schmidt et al. 2014; Treu et al. 2015) imaging. The blue, green, and red channels are composed by the labeled filters on the right. The white arrows point to the two BCGs (NE and SW) which are separated by $\Delta V_{r.f.} \sim 900 \text{ km s}^{-1}$ (Balestra et al. 2015), and are likely in a merging state (Mann & Ebeling 2012; Jauzac et al. 2015b; Ogrea et al. 2015). The two distinct P.A.s of the spectroscopic GLASS pointings are shown by the green (P.A.=164°) and red (P.A.=247°) squares. The cyan square outlines the area show in Figure 3. The locations of the emission line objects from Table 3 are marked by circles, with color coding reflecting the GLASS spectroscopic redshift quality (cf. “Quality” in Table 3; 3=orange, 4=magenta) and labels given by GLASS IDs. There are a few objects that fall outside of the direct image FOV. Their spectra were dispersed onto the chip, so they were still able to be extracted and analyzed (see Figure 2).

images lacking spectra and received an average grade of > 1 but < 1.5 . Images lacking spectra and receiving an average grade of ≥ 1.5 were not used by the modeling teams.

For our lens model, we decided to only consider multiple images in the Gold and Silver categories, which included 80/31 total multiple images/systems. In order to use a Silver multiple image in the lens model, it was necessary to estimate its redshift. Because the grading was done via visual inspection, it was not guaranteed that every multiple image would be detected in our photometric catalog. Of the 31 systems comprising

Gold and/or Silver images, only 26 were included in our lens model. Five systems (systems 8, 33, 40, 41, and 51, all are graded Silver) are not included in our model due to problems with photometry and redshift. Neither of the two Silver images in system 8 was detected in the photometric catalog, most likely due to their faintness and proximity to bright cluster members. Systems 33, 40, and 51 had poorly constrained photometric redshift PDFs. Only a single image in system 41 was detected in the photometric catalog, and its redshift was too poorly constrained to use in the lens model. The redshift PDFs for the multiple images in systems 33, 40,

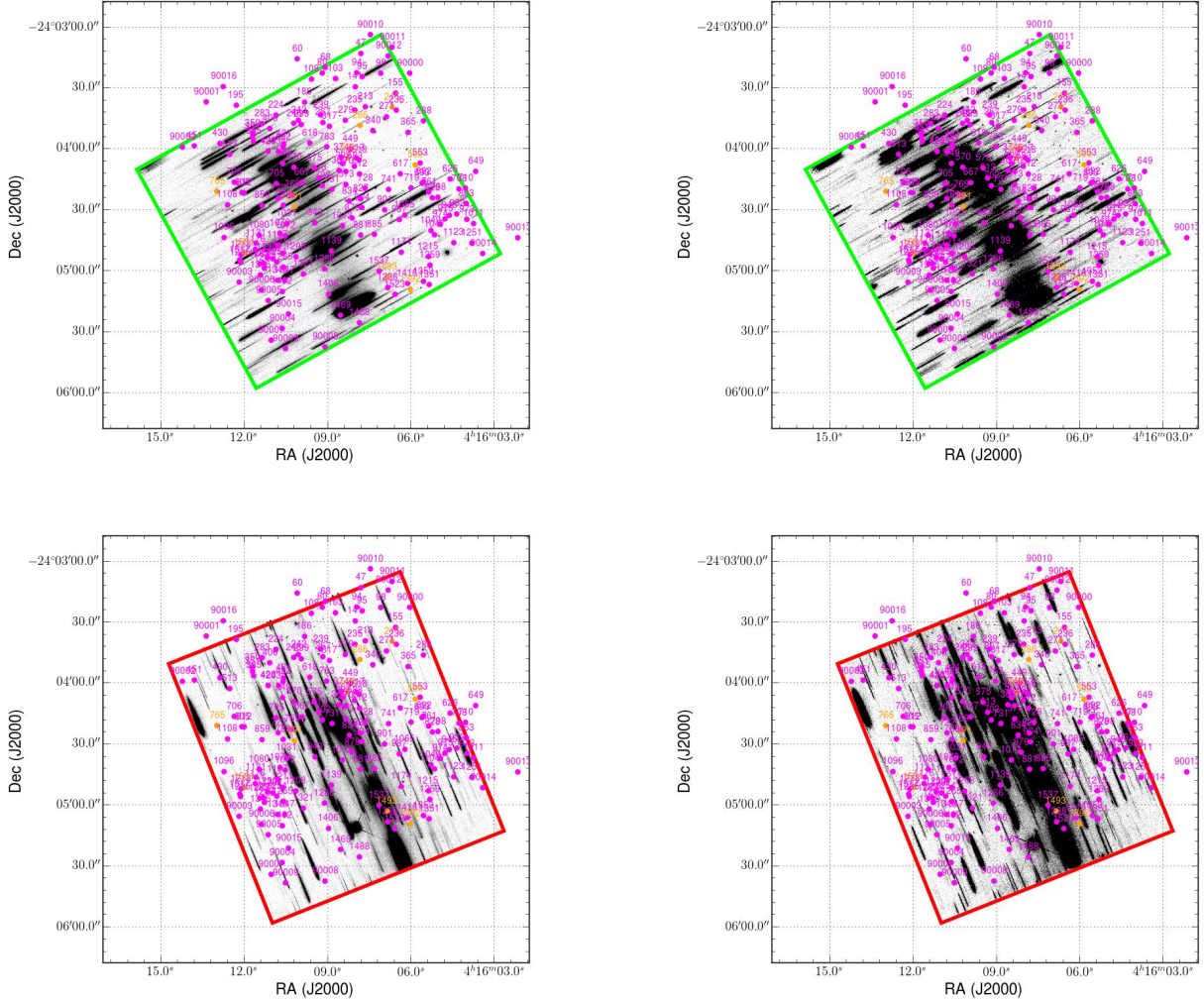


FIG. 2.— The GLASS G102 (left) and G141 (right) grism pointings of MACSJ0416 at two distinct P.A.s, with field-of-view shown by the green (P.A.=164°) and red (P.A.=247°) squares. The circles in all panels denote the positions of the emission line objects identified in this work (Table 3), with color coding and labels following the conventions adopted in Figure 1. The circles that fall outside of the grism pointings are identified in HST images with a larger FOV than the individual grism FOVs. These objects can still be observed in the grism data because their first order spectra are dispersed onto the chip.

41, and 51 are shown in Appendix A. For the remaining Silver images, it was necessary to compute photometric redshifts to include them in the lens model. For these systems we used photometric redshifts obtained by the ASTRODEEP team (Castellano et al., 2015, submitted; Merlin et al. 2015, submitted). The ASTRODEEP photometric redshifts were obtained through χ^2 minimization over the observed *HST*+IR HFF bands using PEGASE 2.0 (Fioc & Rocca-Volmerange 1997). For more details see Castellano et al., (2015, submitted) and Merlin et al. (2015, submitted). The ASTRODEEP catalogs were built after subtracting ICL emission and the brightest foreground galaxies from the images in order to maximize the efficiency of high-redshift source detection and to obtain unbiased photometry. The catalogs employed the seven HFF filters: F435W, F606W, F814W, F105W, F125W, F140W, and F160W, a HAWK-I *K*-band image (G. Brammer, in prep), and *Spitzer* IRAC [3.6] and [4.5] channels. The ASTRODEEP catalogs used two dif-

ferent detection images to create separate photometric catalogs. One catalog used F160W as the detection image, whereas the other used a stacked NIR image. To maximize the number of multiply imaged galaxies that we could detect, we merged the two catalogs into a single photometric catalog for this work.

Combining the photometric redshift information for multiple images of the same source provides a tighter constraint than a single measurement. We used a hierarchical Bayesian method similar to that used in Wang et al. (2015) (see also Press 1997 and Dahlen et al. 2013) to combine the multiple photometric redshift probability density functions for each image of a source $P_i(z)$ into one $P(z)$ for each source. We used the peak of the combined $P(z)$ (hereafter referred to as z_{Bayes}) as input to the lens model. In summary, the hierarchical Bayesian method considers the concept of the probability that each input $P_i(z)$ is unreliable (p_{bad}). It uses an input $P_i(z)$ in the calculation of the combined $P(z)$ for the system

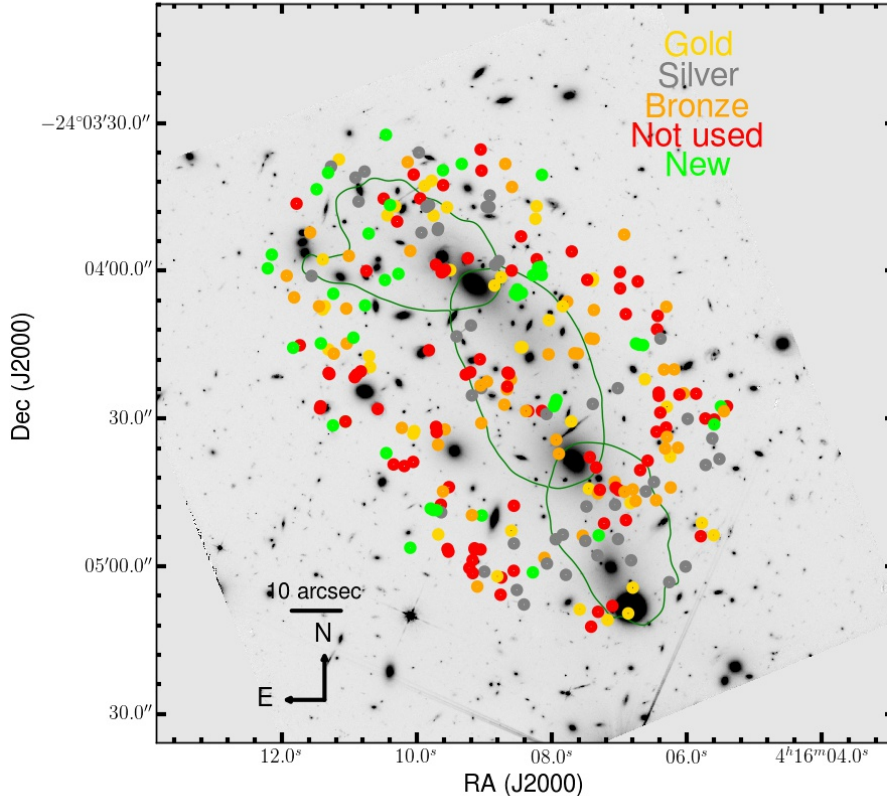


FIG. 3.— All multiple images discovered to date in MACSJ0416. As indicated in the key: gold, gray and orange colored circles correspond to the multiple images in the Gold, Silver and Bronze samples, respectively (Section 4). Red circles correspond to multiple images which the HFF modeling teams deemed were less secure than those in the bronze sample so were not used in the lens models. Green circles represent new multiple image candidates discovered after the grading effort took place. The dark green line is the critical curve from our best-fit lens model at $z = 2.36$, the mean source redshift of the multiple images that were used in our lens model. Shown is the co-added CLASH+HFF+GLASS F105W image.

if it is reliable, otherwise it uses a flat (noninformative) $P_i(z)$. The method then marginalizes over all values of p_{bad} using an assumed prior on p_{bad} to calculate the posterior $P(z)$ for the entire system. We assume a flat prior in p_{bad} for $p_{\text{bad}} \leq 0.5$, i.e., that each $P(z)$ has at least 50% chance of being informative. This has the effect that for some systems with two images, the posterior $P(z)$ of the system has a small but non-zero floor due to the contribution from a noninformative $P_i(z)$. Because the floor inflates the photometric redshift uncertainty, we subtract the floor from all posterior $P(z)$'s before calculating confidence intervals. Subtracting the floor does not change the peak redshift of the posterior $P(z)$.

4.2. GLASS spectroscopy

The GLASS spectroscopic data were carefully examined for a total of 272 multiple image candidates in the attempt to measure spectroscopic redshifts. Each spectrum was visually inspected by multiple investigators (A.H., T.T., and A.B.) using the GLASS Graphical User Interfaces (GUIs) dubbed the GLASS Inspection GUI (GiG) and GLASS Inspection GUI for redshifts (GiGz⁷;

Treu et al. 2015). Both P.A.s were inspected individually and then again once stacked together. The results were then combined to form a list of multiple images with identified emission lines. Following GLASS procedure (Schmidt et al. 2015; Treu et al. 2015), a quality flag was given to the redshift measurement: $Q=4$ is secure; $Q=3$ is probable; $Q=2$ is possible; $Q=1$ is likely an artifact. As described in Treu et al. (2015), these quality criteria take into account the signal to noise ratio of the detection, the probability that the line is a contaminant, and the identification of the feature with a specific emission line. For example, $Q=4$ is given for spectra where multiple emission lines are robustly detected; $Q=3$ is given for spectra where either a single strong emission line is robustly detected and the redshift identification is supported by the photometric redshift, or when more than one feature is marginally detected; $Q=2$ is given for a single line detection of marginal quality. As shown in Table 3, new spectroscopic redshifts were obtained for Quality 4 and 3 measurements only, consisting of 31 images in total, corresponding to 16 systems. The spectra of these objects are shown in Figs. B1–B24.

The uncertainty in our spectroscopic redshift measurements is limited by the grism wavelength resolution of

⁷ Available at <https://github.com/kasperschmidt/GLASSinspectionGUIs>

approximately 50Å and by uncertainties in the zero point of the wavelength calibration. By comparing multiple observations of the same object we estimate the uncertainty of our measurements to be in the order of $\Delta z \lesssim 0.01$, similar to what was reported by Wang et al. (2015).

Some multiple images that we confirm with GLASS spectroscopy were previously spectroscopically confirmed by other authors. We compare the redshifts obtained in this work to those previously obtained, seeing agreement within the uncertainties for all multiple images except system 14. Images 14.1, 14.2, and 14.3 were originally reported to be spectroscopically confirmed at $z = 2.0531$ by Richard et al. (2014), using incomplete CLASH-VLT data. Grillo et al. (2015), using the complete CLASH-VLT data set for MACSJ0416, recently reported redshifts of $z = 1.6370$ for images 14.1 and 14.2. We confirm the updated redshift measurements of 14.1 and 14.2 by Grillo et al. (2015) by identifying strong [O II] $\lambda\lambda 3727, 3729$ and [O III] $\lambda\lambda 4959, 5007 + H\beta$ emission at $z_{\text{grism}} = 1.63 \pm 0.01$ in the GLASS spectra of both images. In addition, we confirm 14.3 at $z_{\text{grism}} = 1.63 \pm 0.01$ by identifying the same lines observed in the grism spectra of 14.1 and 14.2 (see Figures B14–B16). We note that all v1 lens models of the cluster that used system 14 used the incorrect spectroscopic redshift of $z = 2.0531$.

Using the GLASS spectroscopy, we confirm the redshifts of 13 multiple images for the first time. These are multiple images 5.1, 5.2, 5.3, 5.4, 12.3, 15.1, 23.1, 23.3, 26.1, 27.2, 28.1, 28.2, and 29.3 in Table 2. We show the GLASS spectra for these objects in Appendix B, with the exception of 12.3, 28.1 and 28.2 which are available in an online grism catalog⁸. All spectra are also available in an online catalog⁸. Before the GLASS data were analyzed, none of the images in system 5 had published spectroscopic redshifts. We confirm all four images in the system as belonging to the same source galaxy to $z = 2.09 \pm 0.01$ based on the detection of [O III] $\lambda\lambda 4959, 5007$ in both P.A.s of the G141 spectra of all four images. $H\beta$ and [O II] $\lambda\lambda 3727, 3729$ were also detected in 5.1, 5.2, and 5.3, consistent with $z = 2.09 \pm 0.01$. The CLASH-VLT team published a consistent redshift of $z = 2.092$ (Balestra et al. 2015) for image 5.2 after the HFF modeling team determined its samples using the GLASS spectra. 12.3 was the only multiple image candidate inspected with significant continuum emission in the GLASS spectra, but no emission lines were apparent. It was confirmed to $z = 1.96 \pm 0.02$ by fitting its bright continuum emission in the GLASS spectra to template SEDs using the method described by G. Brammer, (in prep.). 15.1 was confirmed to $z = 2.34$ by the detection of [O III] $\lambda\lambda 4959, 5007$ in both P.A.s of the G141 spectra. 23.1 and 23.3 were confirmed to $z = 2.09 \pm 0.01$ by the detection of strong [O III] $\lambda\lambda 4959, 5007$ in both P.A.s of the G141 spectra. We confirmed 26.1 to $z = 2.18 \pm 0.01$ by the detection of [O II] $\lambda\lambda 3727, 3729$ and [O III] $\lambda\lambda 4959, 5007$ in both P.A.s of the G141 spectra. We detected [O III] $\lambda\lambda 4959, 5007$ at $z = 2.11 \pm 0.01$ in both P.A.s of the G141 spectra of image 27.2. 28.1 and 28.2 were blended in the segmentation map used to extract grism objects. Like multiple image 12.3, 28.1 and 28.2 were confirmed by fitting the bright continuum emission in the GLASS spectra to template SEDs, finding a best-fit redshift of $0.938^{+0.001}_{-0.002}$.

29.3 was confirmed by detecting [O III] $\lambda\lambda 4959, 5007$ at $z = 2.28 \pm 0.01$ in both G141 P.A.s. The catalog of multiply imaged objects with GLASS redshifts is publicly available^{3,8}.

4.3. Visual search in GLASS data

We also conducted a search for line emitters among known sources within the entire grism field-of-view. Two co-authors (A.B. and T.T.) visually inspected all of the 2D grism spectroscopic data products, the contamination models, and residuals after contamination subtraction. The grism spectra extraction is based on a public HFF photometric catalog available on the STScI MAST archive⁹, supplemented by our own photometric catalogs based on CLASH images and GLASS direct images. We attempted to identify new multiple systems among the galaxies with the same grism spectroscopic redshifts but did not find any. Some of them are ruled out because of the relative positions of the multiple images in the cluster, while others are ruled out because their distinct colors and morphologies are inconsistent with being the same source.

We compiled a list of singly-imaged galaxies with redshifts determined from both emission-line and absorption features, consisting of 4, and 166, quality 3 and 4 spectroscopic redshift measurements respectively, which are color coded in Figure 1 and Figure 2 and listed in Table 3. Using the photometric catalog described above, we measure the photometric redshifts of these objects and compare them with the spectroscopic redshifts. A comparison is displayed in Figure 4. Of the objects for which photometric redshifts could be measured, we find that approximately 66% (57/86) of the photometric redshifts agree within their 68% confidence limits uncertainties with the corresponding spectroscopic redshifts. This suggests that the photometric redshift errors are reliably estimated.

5. GRAVITATIONAL LENS MODEL

Our lens modeling method, SWUnited (Bradač et al. 2005, 2009a), constrains the gravitational potential of a galaxy cluster via an iterative χ^2 minimization algorithm. It takes as input a simple initial model for the potential. After each iteration, a χ^2 is calculated from strong and weak gravitational lensing data on an adaptive, pixelated grid. The number of grid points is increased at each iteration, and the χ^2 is recalculated. Once the minimum is found, and convergence is achieved, derivative lensing quantity maps, such as convergence (κ), shear (γ) and magnification (μ), are produced from the best-fit potential map.

The strong lensing constraints on the lens model are described in (4). Our weak lensing catalog is based on the ACS/WFC F606W observations ($\sim 30ks$) of the cluster from the HFF program. Using the HFF image results in a factor of two increase in the source density of weak lensing galaxies compared to the CLASH imaging. For the reduction and weak lensing catalog generation we make use of the pipeline described by Schrabback et al. (2010), which employs the KSB+ formalism (Kaiser et al. 1995; Luppino & Kaiser 1997; Hoekstra

⁸ Available at http://www.stsci.edu/~brammer/GLASS_zcat/

⁹ <https://archive.stsci.edu/prepds/frontier/>

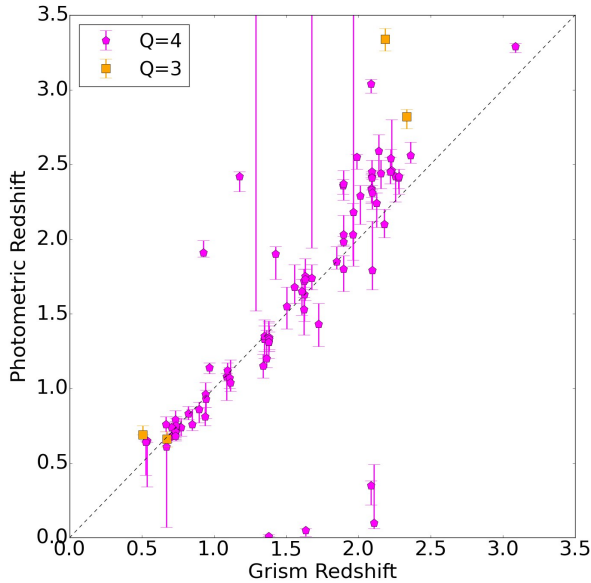


FIG. 4.— Comparison between the grism and photometric redshifts for the 86 objects with high-confidence emission lines (quality flags 4 (magenta pentagons) or 3 (orange squares)) for which photometric redshifts could be measured. Error bars on the photometric redshifts are 1σ (enclosing 68% of the total probability). There is good statistical agreement between photometric and grism redshifts, with 57/86 (66%) of the grism redshifts within the photometric redshift error bars. This suggests that the photometric redshift errors are well-estimated. The dotted black line is shown for reference and represents perfect agreement between photometric and grism redshifts.

et al. 1998) for galaxy shape measurements as detailed by Erben et al. (2001) and Schrabbach et al. (2007). A major difference compared to Schrabbach et al. (2010) is the application of the pixel-based correction for charge-transfer inefficiency (CTI) developed by Massey et al. (2014). Our modeling of the temporally and spatially variable ACS point-spread function is based on the principal component analysis developed by Schrabbach et al. (2010), which we recalibrate using F606W stellar field observations taken after Servicing Mission 4. Further details on the recent pipeline modifications are provided by Schrabbach et al. (in prep.), including a new verification test for the CTI correction in the context of cluster weak lensing studies and updates for the employed weak lensing weighting scheme. Weak lensing galaxies were individually assigned a redshift using the ‘ZBEST’ keyword in the ASTRODEEP photometric catalog (see section 4.1), or the CLASH photometric catalogs for galaxies outside of the HFF *HST*+IR bands. The CLASH photometric catalogs use the Bayesian Photometric Redshifts (BPZ) code (Benítez 2000). We use the ‘ z_b ,’ the most likely redshift given by BPZ, to estimate the redshifts of the weak lensing galaxies. We only use galaxies with $z_b > z_{\text{cluster}} + 0.2$ to ensure that the majority of the catalog contains background galaxies.

Maps of the convergence and magnification for a source at $z = 9$ are shown in Figure 5. The convergence map exhibits two peaks, roughly centered at the positions of the two brightest cluster galaxies (BCGs). Smaller substructures can be seen to the northeast of the NE BCG and to the south of the SW BCG. The magnification

map shows that the critical curve, the curve along which the magnification is maximized is very elliptical. The magnification reaches values up to $\mu \sim 10 - 20$ within a few arcseconds from the critical curve and values of $\mu \sim 1 - 2$ near the edge of the HFF footprint. Typical values of the magnification are $\mu \sim 1 - 5$ throughout the HFF footprint.

5.1. Comparison with previous work

A previous model of MACSJ0416 using pre-HFF data was created using the same lens modeling code used in this work. The previous model was created in response to a call by STScI to model the HFF clusters before the HFF images were taken. The previous model appears on the publicly accessible HFF lens modeling website as the Bradač v1 model¹⁰. Our previous model was constrained using 46 total multiple images belonging to 12 distinct systems, as opposed to the 72 images and 26 systems used in the model presented here, which is also made available to the public on the HFF lens modeling website as the Bradač v3 model. Only a few modeling teams produced v2 lens models of MACSJ0416. The v2 HFF models were submitted to STScI during the time between the two official calls for lens models. Because our team submitted lens models exclusively during the official lens modeling calls, only Bradač v1 and v3 models exist of MACSJ0416. In the v1 model, magnification uncertainties were estimated by bootstrap-resampling the weak lensing galaxies. In this work, however, we took a different approach to estimate uncertainties, one that we expect more accurately represents the statistical uncertainties. Because the number of multiple image systems used in this model is a factor of two larger than in the v1 model, we bootstrap-resampled all of the multiple image systems used in the model that were not spectroscopically confirmed. These are the systems for which we use z_{Bayes} in the lens model. We assessed the impact of photometric redshift uncertainty on the derived lensing quantities by resampling the redshift of each system lacking spectroscopic confirmation from their full z_{Bayes} posteriors. We exclude values of the redshift $z < (z_{\text{cluster}} + 0.1)$ when resampling from the z_{Bayes} posteriors. We compare the variance in magnification due to redshift uncertainty with the variance in magnification due to bootstrap-resampling the multiple image systems, finding that the latter is dominant. We nonetheless propagate both sources of error when reporting the errors on all derived lensing quantities in this work. Systematic uncertainties are not accounted for in our error analysis.

Six other teams (CATS, Sharon, Zitrin, Williams, GLAFIC, and Diego, as they appear on the HFF lens modeling page) created new lens models of the HFF clusters, which have also been made available to the public on the HFF lens modeling website¹⁰. The lens models were released to the public on Dec 4, 2015 while we were preparing this manuscript, but after we had completed the lens model of the cluster. All teams had access to the same multiple image constraints, including the spectroscopic constraints from GLASS described herein.

¹⁰ <http://www.stsci.edu/hst/campaigns/frontier-fields/Lensing-Models>

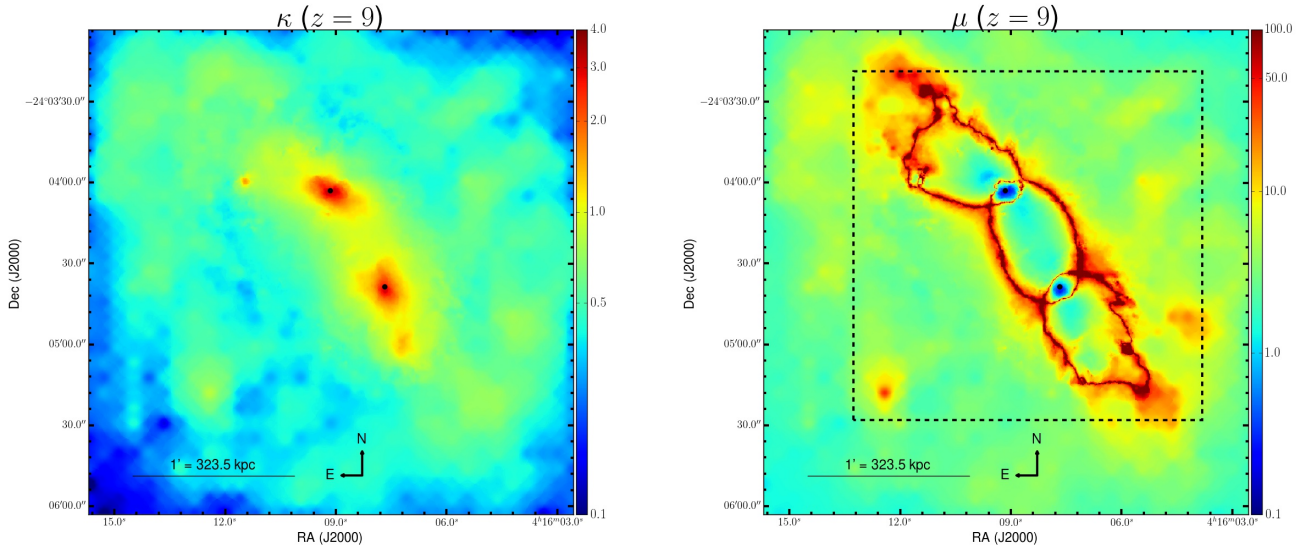


FIG. 5.— **Left** - Convergence (κ) map of MACSJ0416 produced by our lens model for a source at $z_s = 9$. The convergence map reveals two primary total mass density peaks, centered approximately at the location of the two BCGs, which are marked by the two black points. **Right** - Flux magnification (μ) map of MACSJ0416 produced by our lens model for a source at $z = 9$. The approximate location of the critical curve, the curve along which magnification is maximized, can be seen. The dotted black square outlines the common area over which magnification maps were produced by all collaborative HFF modeling teams (see 5.1; Figure 6). Both the convergence and the magnification maps reveal a highly elliptical total mass distribution, as found by several other authors (e.g. Zitrin et al. 2013; Jauzac et al. 2014). Both maps cover the same $3.0 \times 3.0 \text{ arcmin}^2$ footprint. The two black points on each map mark the centers of the two BCGs determined from the F105W image. Note that the colorbar is log-scale.

The CATS (v3), Diego, Zitrin (nfw and ltm-gauss), and Williams (v3) models use the same Gold and Silver multiple images that we used to constrain our model. The CATS (v3.1), Williams (v3.1) and GLAFIC models use Gold, Silver and Bronze images, and the Sharon model uses only the Gold images. We expect that the four models that used Gold and Silver images are the most directly comparable to our lens model.

While the determination of the Gold, Silver and Bronze samples was coordinated among the modeling teams, the determination of the redshifts of the images lacking spectroscopic confirmation, i.e., the Silver and Bronze images, was not. Each team independently determined the redshifts of the Silver images. As a result, no two models, with the exception of the Zitrin nfw and ltm-gauss models, share the exact same multiple image constraints. This should be kept in mind when comparing the models.

We first compare the cumulative magnified $z = 9$ source plane area (cumulative area, hereafter) predicted by all models in Fig. 6. The cumulative area predictions among the nine models are significantly different for magnifications in the range $1 \lesssim \mu \lesssim 5$. As shown in Figure 5, the region with $1 \lesssim \mu \lesssim 5$ is primarily in the outskirts of the field, several hundred kpc from the critical curve. At this distance from the critical curve, weak lensing galaxies provide the only constraints to our model, as the strength of the lens is not sufficient to multiply-image background galaxies. None of the other nine models use weak lensing constraints, but instead rely on an extrapolation of the core region to predict the magnification in the outskirts, therefore the disagreement with our model is not surprising in this regime. We assess whether the use of different sets of images could be responsible for the difference, but find that it is likely not the case. The models that similarly used the Gold and Silver samples of multiple images are still in disagreement

in this regime. Further, the CATS and Williams teams constructed two models of the cluster. The v3 models of both teams use the Gold and Silver images only, whereas the v3.1 models use the Gold, Silver and Bronze samples. For each of these teams, the cumulative area predicted by the v3 and v3.1 models are very similar over a large range of magnifications ($1 < \mu < 100$), despite the v3.1 models using an additional 58 Bronze images. We also test whether the choice of our initial model could bias our model predictions. The prediction from our initial model is significantly different from the prediction from our reconstructed model. In fact, the initial model is more similar to the CATS, GLAFIC and Zitrin models for magnifications in the range $1 \lesssim \mu \lesssim 5$, and it is driven away from these models during the minimization. There is general agreement among the models for cumulative areas at $\mu \gtrsim 5$. This is reassuring because the region of the cluster for which $\mu \gtrsim 5$ is near the critical curve, which is primarily constrained by the multiply imaged galaxies, which are numerous for this cluster and similar among the modeling teams. The image plane area used to make the cumulative area plots was the common area shared by all nine magnification maps, and is shown as the dashed box in the right panel of Figure 5. This area was set by the Williams magnification maps, which are approximately 4.65 arcmin^2 .

Although different modeling teams used different sets of multiply imaged galaxies, it is difficult to see how this directly affects the models using the cumulative area plot. The factor with which the deflection angle scales for a source at $z = z_{\text{Bayes}}$ is the ratio of the angular diameter distances, $\frac{D_{\text{ds}}}{D_s}(z_1, z_s)$, where D_{ds} is the angular diameter distance between the lens at $z = z_1$ and the source at $z = z_s$, and D_s is the angular diameter distance between $z = 0$ and $z = z_s$. It is therefore the factor in which

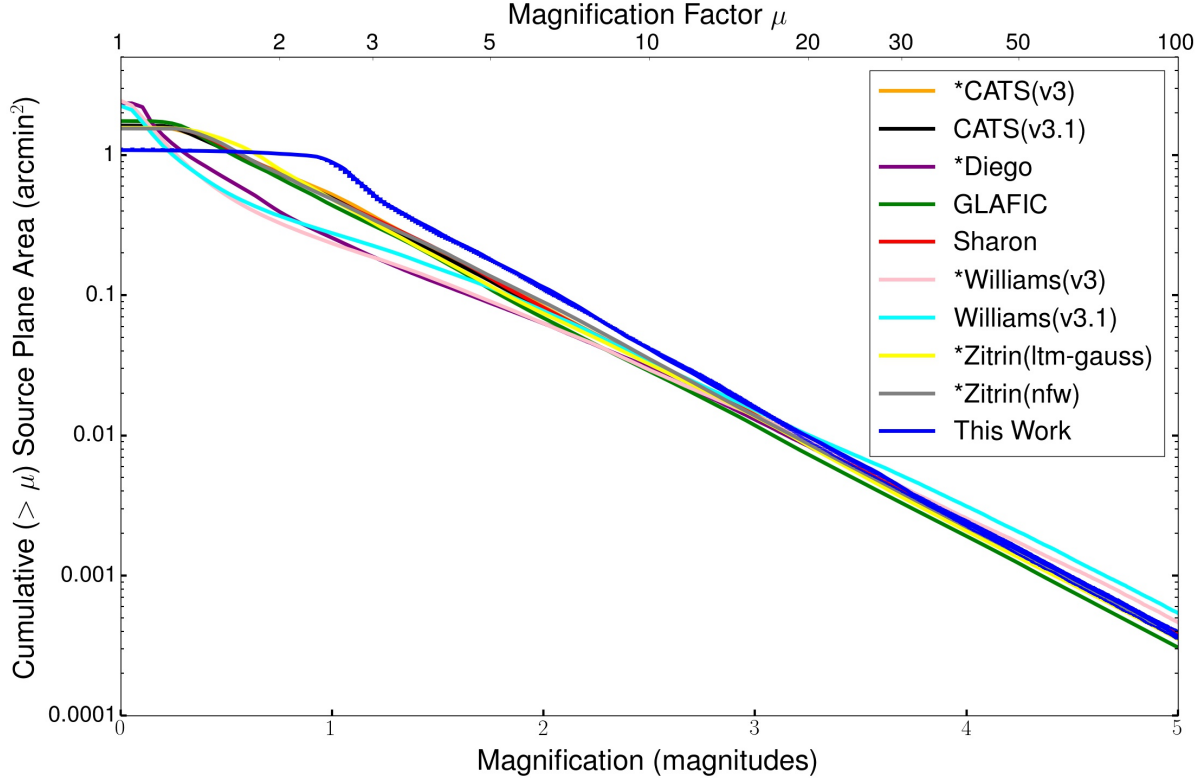


FIG. 6.— Cumulative source plane area (“cumulative area”) versus magnification at $z = 9$ for the lens model determined in this work (Bradac v3) and the other nine v3 HFF lens models. Model names preceded by “*” indicate models using the same sample of multiply imaged galaxies as used in this work, although the redshifts of the galaxies lacking spectroscopic confirmation have been estimated differently (see 5.1 for more details). The models are in general agreement at large magnifications ($\mu \gtrsim 5$). This is not surprising given that the multiple image constraints appear in the regions with large magnification near the core of the mass distribution. There is significant disagreement among the models at $1 \lesssim \mu \lesssim 5$. These values of magnification are indicative of the outskirts of the modeled area of the cluster, where constraints come from weak lensing alone. Only our model uses weak lensing constraints. 68% confidence vertical error bars are shown for our model only and are approximately the thickness of the line.

the source redshift for a multiple image system directly enters the lens model. In Figure 7, we compare this ratio for redshifts estimated in this work to those predicted by the CATS v3.1 lens model. We choose to compare to the CATS v3.1 model because it uses Gold, Silver and Bronze images and therefore provides the largest number of redshifts with which we can compare our photometric redshifts. The comparison is done for multiple image systems for which no spectroscopic redshift has been measured, whether in this work or previously. In this way, no spectroscopic redshift could be used as a prior for predicting the redshift. In the figure, z_{model} is the redshift the CATS team obtained by optimizing their lens model while leaving the redshift as a free parameter. Overall, z_{Bayes} and z_{model} agree within the uncertainties. Wang et al. (2015) reached a similar conclusion by comparing z_{Bayes} and z_{model} for the multiple images predicted by the CATS v2 lens model of the HFF cluster Abell 2744. This is encouraging because similar inputs to the models allow a more direct comparison of the results.

6. STELLAR MASS FRACTION

6.1. Stellar mass density map

The lens model provides an estimate for the total mass density of the cluster, composed of mostly invisible dark matter. A fractional component of the total mass density

comes from stars and can be inferred from the observed stellar light, independently from the lens model. The *Spitzer* IRAC $3.6 \mu\text{m}$ image samples close to rest-frame K -band for the cluster, so we use the $3.6 \mu\text{m}$ fluxes from cluster members to estimate the cluster stellar mass distribution. The cluster members come from the selection by Grillo et al. (2015), consisting of 109 spectroscopically confirmed and 66 photometrically selected cluster members.

To create an image with $3.6 \mu\text{m}$ flux from cluster members only, we first create a mask with value 1 for pixels that belong to cluster members in the F160W image and 0 otherwise. We then convolve the mask with the $3.6 \mu\text{m}$ PSF to match the IRAC angular resolution, set the pixels below 10% of the peak value to zero, and resample the mask onto the IRAC pixel grid. We obtain the $3.6 \mu\text{m}$ map of cluster members by setting all IRAC pixels not belonging to cluster members to zero and smoothing the final surface brightness map with a two-pixel wide Gaussian kernel.

The IRAC surface brightness map is transformed into a stellar surface mass density map (stellar mass density map, hereafter) by first converting the $3.6 \mu\text{m}$ flux into a K -band luminosity map. The luminosity map is then multiplied by the stellar mass to light ratio derived by Bell et al. (2003) using the so-called “diet” Salpeter stellar initial mass function (IMF), which has 70% of the

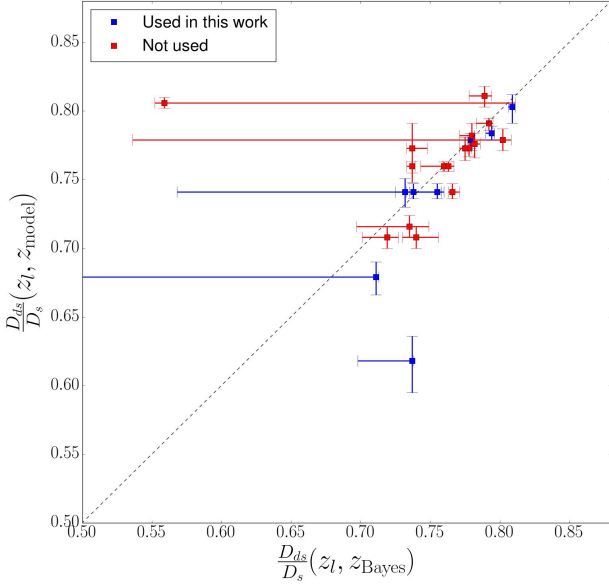


FIG. 7.— Comparison of the ratio of angular diameter distances, the quantity with which the lensing deflection scales, for redshifts of multiply imaged galaxies determined in this work (z_{Bayes}) versus the redshifts predicted by the CATS v3.1 model (z_{model} ; Jauzac et al. in prep.). The CATS v3.1 model used Gold+Silver+Bronze images, whereas we only used Gold+Silver images in our lens model, although we calculate z_{Bayes} for all three categories to improve the statistics for this comparison. Gold+Silver images are the blue points, and the Bronze images are the red points. The vertical error bars were obtained by resampling from the 1σ Gaussian errors on z_{model} . The horizontal error bars represent 68% confidence and were obtained by resampling from $P(z_{\text{Bayes}})$. The asymmetric horizontal error bars arise because $P(z_{\text{Bayes}})$ is multi-modal for those multiply imaged galaxies. There is overall good agreement between z_{Bayes} and z_{model} . The dotted black line is shown for reference and represents perfect agreement.

mass of the Salpeter (1955) IMF due to fewer stars at low masses. Bell et al. (2003) obtained a stellar mass to light ratio of $M_*/L = 0.95 \pm 0.26 M_\odot/L_\odot$ in the stellar mass bin $10 < \log(M_* h^2) < 10.5$. Their M_*/L values are insensitive to the chosen stellar mass bin. The $\sim 30\%$ error on M_*/L is the largest source of statistical uncertainty in the stellar mass density map.

The main source of systematic uncertainty in the stellar mass density map is the unknown initial mass function (IMF). For example, if we adopt a Salpeter (1955) IMF, as suggested by studies of massive early-type galaxies, the stellar mass density increases by a factor of 1.55 everywhere. We also assess the cluster member selection as a source of systematic uncertainty. Grillo et al. (2015) estimate that their cluster member catalog is $\gtrsim 95\%$ complete down to a stellar mass of $\log(M_*/M_\odot) \simeq 9.8$ within the CLASH F160W footprint. We estimate the fraction of stellar mass density not included in our analysis due to the incomplete cluster member selection at lower stellar masses. We compare the integral of the stellar mass function obtained by Annunziatella et al. (2014) for MACS J1206.2-0847, another CLASH cluster at similar redshift ($z = 0.44$), over the range of complete stellar masses from the Grillo et al. (2015) selection to the integral

over all stellar masses. We find that we only exclude $\sim 3\%$ of the stellar mass within the F160W footprint from CLASH as a result of the incomplete cluster member selection. Grillo et al. (2015) select cluster members down to $\log(M_*/M_\odot) \simeq 8.6$, yet with $< 95\%$ completeness in the stellar mass range $8.6 \lesssim \log(M_*/M_\odot) \lesssim 9.8$. Therefore, the $\sim 3\%$ estimated loss in stellar mass is a slight overestimate of the loss due to the incomplete cluster member selection. The presence of the ICL, when not accounted for, can also cause the stellar mass density to be underestimated (e.g. Gonzalez et al. 2013). Burke et al. (2015) recently measured the fraction of total cluster light contained in the ICL for 13/25 CLASH clusters, including MACSJ0416. For MACSJ0416, they found that $2.69 \pm 0.10\%$ of the total cluster light is contained in the ICL. Both the stellar mass incompleteness and ICL act to decrease the measured stellar mass density. Both effects, however, are an order or magnitude smaller than the uncertainty due to the IMF and the stellar mass to light ratio obtained by Bell et al. (2003).

6.2. Stellar to total mass ratio

We obtain the projected stellar to total mass ratio (f_* , hereafter) map by dividing the stellar mass density map obtained from photometry by the total surface mass density map (total mass density, hereafter) obtained from our lens model. Before division, we match the resolutions of the two maps. The stellar mass density map resolution is controlled by the *Spitzer* IRAC $3.6 \mu\text{m}$ imaging resolution, which is roughly uniform across the field. On the other hand, the resolution of the total mass density varies considerably across the field as a result of two processes that occur during the lens modeling procedure. The first effect is regularization, which globally degrades the resolution of the total mass density map. In order to estimate the decrease in resolution due to regularization, we used a simulated galaxy cluster designed to match the data quality of the HFF, Hera (Meneghetti et al., in preparation). We made our own lens model of Hera that includes the effects of regularization, which we compare to the correct lensing maps from the simulation (M. Meneghetti, private communication). The correct simulated lensing maps are of a uniform resolution that is higher than the resolution of our lensing maps. To determine the global resolution correction, we variably degrade the resolution of the simulated convergence map until we find the best match to our reconstructed convergence map. The second effect is non-uniformity in the grid introduced by the lens modeler to match the S/N of the lensing measurements (Bradač et al. 2009b). The process of increasing the resolution in this manner will be referred to as refinement hereafter. Each pixel in the lensing map has an associated refinement level. The refinement grid for MACSJ0416 has four levels: 1, 2, 4 and 8. Level 1 refinement represents no refinement and is reserved for the outskirts of the cluster. Level 8 refinement is applied in a circular region centered on the multiple images used in the lens model with radii equal to 2.4 arcseconds. Refinement levels 2 and 4 are used to mitigate discontinuities between level 1 and level 8 refinement. Refinement level 4 is used around the NE and SW BCG in circles of radii 0.6 and 0.45 arcminutes, respectively.

To match the resolution of the stellar mass density map to that of the total mass density map from our lens

model, we convolve the stellar mass density map with a Gaussian kernel of spatially varying width. We vary the kernel width according to the level of refinement at each pixel. The kernel width in refinement level 2 regions is always half the width of the kernel used in refinement level 1 regions. Likewise, the kernel width in refinement levels 4 and 8 are always $\frac{1}{4}$ and $\frac{1}{8}$ of the width of the kernel used in refinement level 1 regions, respectively. We vary the refinement level 1 kernel width from 0 to 1 arcminutes and assess the squared difference in the convergence in our reconstruction and the simulated map, finding a best fit kernel width of 0.75 arcminutes in the refinement level 1 region. The stellar mass density map is convolved with the four different kernels in the four refinement regions determined by this value alone. The resulting resolution-corrected stellar mass density map is shown in the left panel of Figure 8.

The f_* map is shown in the right panel of Figure 8. There is significant variation in f_* throughout the cluster. While f_* reaches as high as ~ 0.03 in some places, the global mean within the stellar mass-complete region of the map is 0.009 ± 0.003 (stat.; 68% confidence), after adding in a $2.69 \pm 0.10\%$ ICL contribution to the stellar mass density determined by Burke et al. (2015).

The IMF is largest source of systematic uncertainty in f_* . The choice of a Salpeter (1955) IMF over the diet-Salpeter IMF assumed in this work would lead to an increase in the stellar mass density map, and therefore in f_* , of $\sim 50\%$. Another source of systematic error in f_* is the choice of cosmology, which affects both the stellar mass density and the total mass density. Cosmology impacts the stellar mass density through the distance modulus, which is used to convert the observed surface brightness of cluster members to physical surface brightness. Comparing the distance modulus calculated using our fiducial one-significant-figure concordance cosmology and a two-significant-figure cosmology from (Planck Collaboration 2015, e.g.), we see a difference of $\sim 30\%$. The choice of cosmology has a much smaller effect on the total mass density. Cosmology impacts the total mass density through the critical surface mass density, Σ_c . The difference in Σ_c is $\lesssim 3\%$. The effect of cosmology on Σ_c is not as significant as the effect on the distance modulus because it enters Σ_c in a ratio of angular diameter distances.

We also assess the potential systematic error resulting from smoothing the stellar mass density map to match the resolution of the total mass density map as described above. We show the dependence of f_* on the stellar surface mass density in Figure 9 for two different smoothing approaches. The “auto smoothing” method is the one described above. The “manual smoothing” approach differs from the previous approach in how we estimate the optimal kernel width at each refinement level. In the auto smoothing method, the kernel width in each refinement region is simply $1/l$ times the kernel width in refinement region 1, where l is the refinement level. In the manual smoothing method, however, we determine the optimal kernel width in each refinement region separately. For each refinement level, we mask out the part of the convergence maps not refined at that level before comparing the squared difference in the simulated and reconstructed convergence maps for a range of kernel widths between 0 and 1 arcminutes. In the regions corresponding to re-

finement levels 1 and 2, we find similar kernel widths using both smoothing methods. However, we find much smaller kernel widths in regions corresponding to refinement levels 4 and 8 when using the manual smoothing method. The stellar mass density map is smoothed significantly less near the BCGs in the manual smoothing approach. This effect is illustrated in Figure 9. In the auto smoothing approach, there is a downturn in f_* for stellar surface mass densities $\gtrsim 2 \times 10^{10} M_\odot \text{ kpc}^{-2}$. The downturn is significantly less pronounced in the manual smoothing approach, where the peaks of the stellar mass density are more preserved due to less smoothing. Though a downturn in f_* for stellar surface mass densities associated with the two BCGs could indicate interesting astrophysics, such as decreased star formation efficiency in the BCGs or a varying IMF, it is not robust against the choice of smoothing. The disparity in f_* between the auto and manual smoothing approaches at stellar surface mass densities $\gtrsim 2 \times 10^{10} M_\odot \text{ kpc}^{-2}$ observed in Figure 9 provides an estimate of the systematic error in f_* as a result of smoothing the stellar mass density map. Overall, however, the choice of smoothing approach only affects $\langle f_* \rangle$ by 0.001, sub-dominant to the statistical error on $\langle f_* \rangle$. The trend in f_* with stellar surface mass density for stellar surface mass densities $< 2 \times 10^{10} M_\odot \text{ kpc}^{-2}$ is insensitive to the smoothing approach. This trend holds over $\sim 98\%$ of the area of the stellar mass complete region of the f_* map because values of the stellar surface mass densities exceeding $2 \times 10^{10} M_\odot \text{ kpc}^{-2}$ are rare, only being observed near the peaks of the two BCGs, as can be seen in the left panel of Figure 8. Thus our conclusion that there is considerable variation in f_* throughout the majority of the *HST* WFC3/IR FOV is also insensitive to the systematics associated with smoothing.

We compare our value of $\langle f_* \rangle$ to values obtained in the recent literature. Bahcall & Kulier (2014) measured f_* for $> 10^5$ groups and clusters in the MaxBCG cluster catalog (Koester et al. 2007). Their cluster sample is taken from a photometric redshift range of $0.1 < z < 0.3$. Their f_* measurements cover a large range of scales ($25 \text{ kpc} - 30 h^{-1} \text{ Mpc}$) and total masses ($M_{200} \sim 10^{13} - 10^{15} M_\odot$), where M_{200} is the total mass within r_{200} , the radius within which the mean density is 200 times the matter density of the universe. On all scales larger than a few hundred kpc, Bahcall & Kulier (2014) measure a constant value of $\langle f_* \rangle = 0.010 \pm 0.004$ (68% confidence). For the most massive clusters in their sample, which are most analogous to MACSJ0416, they report a similar value of $\sim 1\%$. Bahcall & Kulier (2014) used stellar mass to light ratios calculated with i-band magnitudes from the Sloan Digital Sky Survey (SDSS; York et al. 2000) while employing a Chabrier IMF. In order to directly compare our results to Bahcall & Kulier (2014), we recalculated $\langle f_* \rangle$ using F105W, the band with the smallest K-correction to SDSS i-band at the redshift of MACSJ0416, and then scaled the resulting light map using the same stellar mass to light ratio that they used, $M_*/L = 2.5$. After recalculating, we obtain a value of $\langle f_* \rangle = 0.012^{+0.005}_{-0.003}$ (stat.; 68% confidence), in agreement with the large scale value obtained by Bahcall & Kulier (2014). Gonzalez et al. (2013) measured f_* for 12 clusters at $z \sim 0.1$ over the mass range $M_{500} = 1 - 5 \times 10^{14} M_\odot$. They measure values of f_* ranging from 5% at the lower

mass end of their sample to 1.5% at the upper mass end. Umetsu et al. (2014) recently measured $M_{500} = 7.0 \pm 1.3 \times 10^{14} M_{\odot}$ for MACSJ0416. We recalculated f_{\star} in the same band (WFPC2 F814W) and using the same stellar mass to light ratio as Gonzalez et al. (2013) ($M_{\star}/L = 2.65$), finding a value of $\langle f_{\star} \rangle = 0.014^{+0.005}_{-0.004}$ (stat.; 68% confidence). While MACSJ0416 is at higher redshift ($z_{\text{cluster}} = 0.396$) and has higher mass than the clusters studied by Gonzalez et al. (2013), our measured value of $\langle f_{\star} \rangle$ for MACSJ0416 is comparable to the values measured by Gonzalez et al. (2013) at the highest masses. We also note that the area in which we calculate f_{\star} is smaller than r_{200} , the radius in which Gonzalez et al. (2013) measured $\langle f_{\star} \rangle$ for their cluster sample. Balestra et al. (2015) measure $r_{200} = 1.82$ Mpc for MACSJ0416. Adopting this value of r_{200} , the region in which we measure f_{\star} is $\sim 0.4r_{200}$. We assumed a 30% error on the values of M_{\star}/L (cf. Bell et al. 2003) when computing $\langle f_{\star} \rangle$ to compare to the values of f_{\star} reported by Bahcall & Kulier (2014) and Gonzalez et al. (2013).

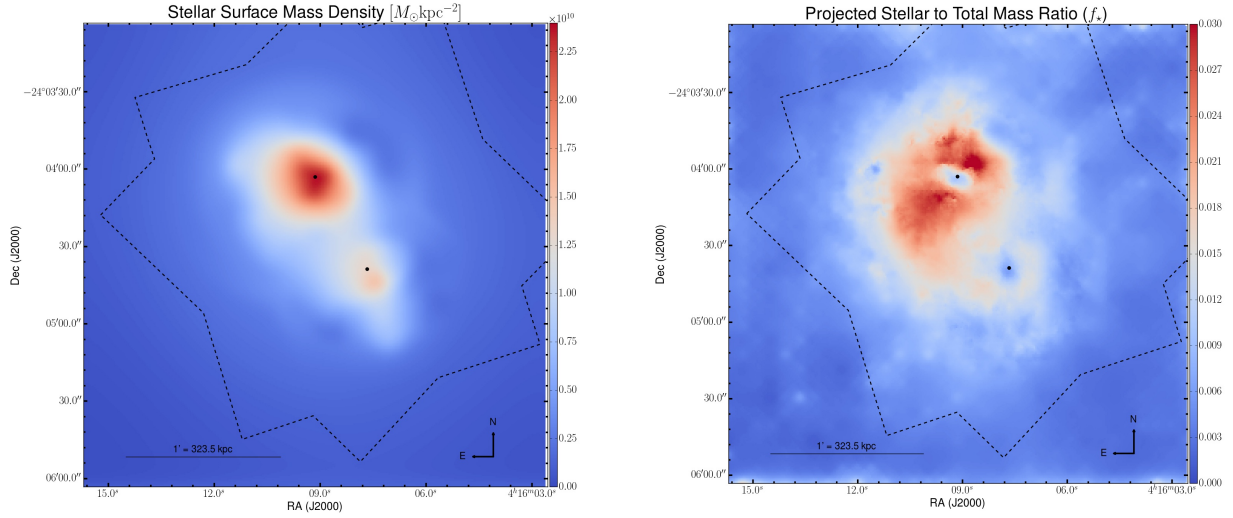


FIG. 8.— **Left** - Stellar surface mass density (in units of $M_{\odot} \text{ kpc}^{-2}$) derived from a *Spitzer*/IRAC [3.6] image of MACSJ0416. The resolution of this map has been matched to the resolution of the total surface mass density map. **Right** - Projected stellar to total mass ratio (f_{\star}), obtained by dividing the stellar surface mass density (left panel) by the total surface mass density obtained from our lens model. The two black points on each map mark the centers of the two BCGs determined from the F105W image (cf. Fig. 5). The dotted black line in both panels shows the dithered F160W footprint from CLASH, which comprises $\sim 5.3 \text{ arcmin}^2$ of the entire 9 arcmin^2 FOV shown. The cluster member selection conducted by Grillo et al. (2015) used to make the stellar surface mass density map is complete down to $\log(M_{\star}/M_{\odot}) \simeq 9.8$ in this region. Outside of this region, the completeness and the uncertainty of both maps are not evaluated.

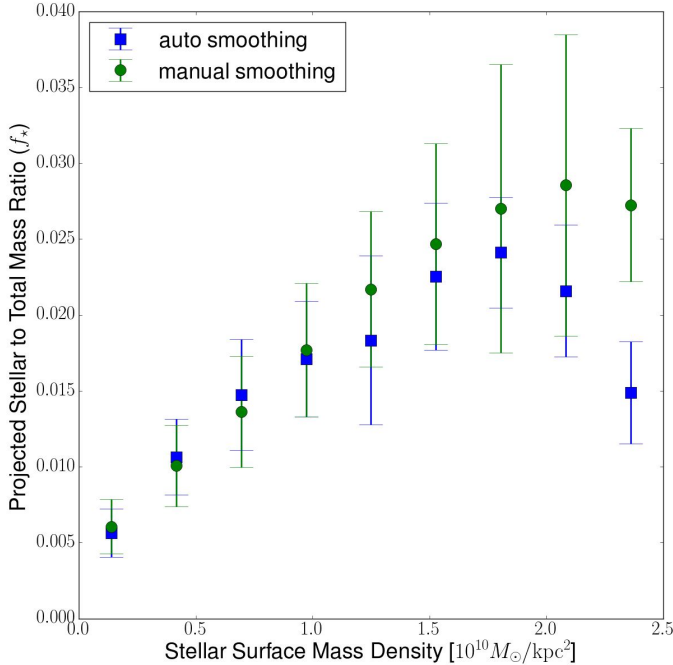


FIG. 9.— Projected stellar mass to total mass ratio (f_{\star}) versus stellar surface mass density (in units of $10^{10} M_{\odot} \text{ kpc}^{-2}$) for the “auto” and “manual” smoothing approaches (described in § 6.2) used to match the resolution of the stellar mass and total mass density maps. The data points and error bars represent the mean and standard deviation of all points falling in each of the equally spaced 9 bins in stellar surface mass density. Only data from within the stellar mass-complete region shown in Figure 8 are displayed in this figure. The two different approaches provide an estimate of the systematic error associated with the resolution matching procedure. The trend in f_{\star} for stellar surface mass densities for $< 2 \times 10^{10} M_{\odot} \text{ kpc}^{-2}$ is bolstered by the agreement between the approaches in this regime. However, at the highest stellar surface mass densities in the cluster, which are found only near the cores of the two BCGs, the two approaches disagree. Thus f_{\star} is too uncertain at stellar surface mass densities $\gtrsim 2 \times 10^{10} M_{\odot} \text{ kpc}^{-2}$ to conclude a downturn, as observed for the auto approach.

7. CONCLUSIONS

The massive galaxy cluster MACSJ0416 is a powerful gravitational lens with excellent constraints for lens modeling. A coordinated search for multiple images of strongly-lensed galaxies performed by several lens modeling teams found ~ 200 candidate multiple images consisting of ~ 100 source galaxies. In order to provide the best constraints to the many lens modeling teams, including our own, we inspected each of these candidate multiple images in the GLASS spectroscopy. Using GLASS spectroscopic measurements together with constraints obtained through the collaborative HFF modeling effort, we produced a gravitational lens model of MACSJ0416. We then compared the projected stellar mass density map derived from IRAC photometry to the total mass density map obtained from our lens model to study the projected stellar to total mass fraction throughout the cluster field. Our main results are summarized here:

1. We have measured spectroscopic redshifts for 31 multiple images (quality flag 3 (probable) and 4 (secure)), confirming 6 multiple image systems for the first time. The spectroscopically confirmed images were used to constrain our gravitational lens models and the nine other lens models discussed in this work. These lens models, including our own, are publicly available¹⁰.
2. We performed a visual search for faint emission and absorption lines, establishing a spectroscopic redshift catalog of weakly-lensed galaxies throughout the primary cluster field. We compared our photometric redshifts with grism spectroscopic redshifts and found good agreement, giving us more confidence in the photometric redshifts (and their errors) of the multiple images. We compared our photometric redshifts with redshifts determined from the v3.1 CATS lens model of MACSJ0416 for the multiple images used in their lens model. We find general agreement with their redshifts.
3. The cumulative magnified source plane area (cumulative area) predicted by our lens model was compared with the nine other lens models of MACSJ0416 constrained using products from the same imaging and spectroscopy data. The cumulative area predictions agree among the models for $\mu \gtrsim 5$ (mostly near the cluster core), but the results diverge among the models for the outlying regions with $\mu \lesssim 5$. We attribute the model differences to the lack of constraints in this region, with the exception of our model which uses weak lensing constraints derived from the HFF imaging data. Despite the conservative approach of including only the Gold (spec- z) and Silver (high confidence phot- z) multiple image systems identified by

the HFF modeling collaboration, systematics from misidentification and redshift estimation of the Silver systems may influence the lens model. However, the inclusion of grism spectroscopic redshifts helps the lens modeling by providing stronger constraints and revising the incorrect redshifts used in the previous models.

4. We obtained a stellar surface mass density map from deep *Spitzer*/IRAC imaging data, using cluster members selected by Grillo et al. (2015). We compare the stellar surface mass density map to the total surface mass density produced from our lens model, producing a map of the projected stellar mass ratio, f_* . There is significant variation in f_* throughout the cluster. f_* increases with stellar surface mass density up to stellar surface mass density of $\sim 2 \times 10^{10} M_\odot \text{ kpc}^{-2}$, above which our results are inconclusive. The global mean projected stellar mass fraction is $\langle f_* \rangle = 0.009 \pm 0.003$ (stat.; 68% confidence) using a diet-Salpeter IMF. We compare our results with recent measurements of $\langle f_* \rangle$ in the literature taken over a wide range of total cluster masses and redshifts. After correcting for different IMFs and filters used to convert stellar light to mass, we find that our measured value of $\langle f_* \rangle$ is broadly consistent with the literature values.

AH acknowledges support by NASA Headquarters under the NASA Earth and Space Science Fellowship Program - Grant ASTRO14F-0007. This work utilizes gravitational lensing models produced by PIs Bradač, Natarajan & Kneib (CATS), Merten & Zitrin, Sharon, and Williams, and the GLAFIC and Diego groups. The lens models were obtained from the Mikulski Archive for Space Telescopes (MAST). This work is based in part on observations made with the NASA/ESA Hubble Space Telescope, obtained at STScI. The data were obtained from MAST. We acknowledge support through grants HST-13459, HST-GO13177, HST-AR13235. MB, KH, and AH acknowledge support for this work through a *Spitzer* award issued by JPL/Caltech. MB and AH also acknowledge support from the special funding as part of the *HST* Frontier Fields program conducted by STScI. STScI is operated by AURA, Inc. under NASA contract NAS 5-26555. TT acknowledges support by the Packard Foundation through a Packard Research Fellowship, and thanks the Osservatorio Astronomico di Monteporzio Catone and the American Academy in Rome for their kind hospitality during the writing of this manuscript. BV acknowledges the support from the World Premier International Research Center Initiative (WPI), MEXT, Japan and the Kakenhi Grant-in-Aid for Young Scientists (B)(26870140) from the Japan Society for the Promotion of Science (JSPS).

REFERENCES

- Annunziatella, M., Biviano, A., Mercurio, A., et al. 2014, *A&A*, 571, A80
Bahcall, N. A., & Kulier, A. 2014, *MNRAS*, 439, 2505
Balestra, I., Mercurio, A., Sartoris, B., et al. 2015, *ArXiv e-prints*, arXiv:1511.02522
Bell, E. F., McIntosh, D. H., Katz, N., & Weinberg, M. D. 2003, *ApJS*, 149, 289
Benítez, N. 2000, *ApJ*, 536, 571
Bertin, E., & Arnouts, S. 1996, *Astronomy and Astrophysics Supplement*, 117, 393
Bradač, M., Erben, T., Schneider, P., et al. 2005, *A&A*, 437, 49

- Bradač, M., Clowe, D., Gonzalez, A. H., et al. 2006, *ApJ*, 652, 937
- Bradač, M., Treu, T., Applegate, D., et al. 2009a, *ApJ*, 706, 1201
- . 2009b, *ApJ*, 706, 1201
- Brammer, G. B., Pirzkal, N., McCullough, P. R., & MacKenty, J. W. 2014, *STScI ISR*
- Brammer, G. B., Ryan, R., & Pirzkal, N. 2015, *STScI ISR* 2015-17
- Brammer, G. B., van Dokkum, P. G., Franx, M., et al. 2012, *The Astrophysical Journal Supplement*, 200, 13
- Burke, C., Hilton, M., & Collins, C. 2015, *MNRAS*, 449, 2353
- Clowe, D., Bradač, M., Gonzalez, A. H., et al. 2006, *ApJ*, 648, L109
- Coe, D., Zitrin, A., Carrasco, M., et al. 2013, *The Astrophysical Journal*, 762, 32
- Dahlen, T., Mobasher, B., Faber, S. M., et al. 2013, *The Astrophysical Journal*, 775, 93
- Diego, J. M., Broadhurst, T., Molnar, S. M., Lam, D., & Lim, J. 2015a, *MNRAS*, 447, 3130
- Diego, J. M., Broadhurst, T., Zitrin, A., et al. 2015b, *MNRAS*, 451, 3920
- Ebeling, H., Edge, A. C., & Henry, J. P. 2001, *ApJ*, 553, 668
- Erben, T., Van Waerbeke, L., Bertin, E., Mellier, Y., & Schneider, P. 2001, *A&A*, 366, 717
- Fioc, M., & Rocca-Volmerange, B. 1997, *A&A*, 326, 950
- Gonzaga, S. 2012, *The DrizzlePac Handbook (STScI)*
- Gonzalez, A. H., Sivanandam, S., Zabludoff, A. I., & Zaritsky, D. 2013, *ApJ*, 778, 14
- Grillo, C., Suyu, S. H., Rosati, P., et al. 2015, *ApJ*, 800, 38
- Hoekstra, H., Franx, M., Kuijken, K., & Squires, G. 1998, *ApJ*, 504, 636
- Jauzac, M., Clément, B., Limousin, M., et al. 2014, *MNRAS*, 443, 1549
- Jauzac, M., Richard, J., Jullo, E., et al. 2015a, *MNRAS*, 452, 1437
- Jauzac, M., Jullo, E., Eckert, D., et al. 2015b, *MNRAS*, 446, 4132
- Johnson, T. L., Sharon, K., Bayliss, M. B., et al. 2014, *ApJ*, 797, 48
- Kaiser, N., Squires, G., & Broadhurst, T. 1995, *ApJ*, 449, 460
- Kawamata, R., Oguri, M., Ishigaki, M., Shimasaku, K., & Ouchi, M. 2015, *ArXiv e-prints*, arXiv:1510.06400
- Koester, B. P., McKay, T. A., Annis, J., et al. 2007, *ApJ*, 660, 239
- Luppino, G. A., & Kaiser, N. 1997, *ApJ*, 475, 20
- Mann, A. W., & Ebeling, H. 2012, *MNRAS*, 420, 2120
- Massey, R., Schrabback, T., Cordes, O., et al. 2014, *MNRAS*, 439, 887
- Merten, J., Meneghetti, M., Postman, M., et al. 2015, *ApJ*, 806, 4
- Momcheva, I. G., Brammer, G. B., van Dokkum, P. G., et al. 2015, *ArXiv e-prints*, arXiv:1510.02106
- Newman, A. B., Treu, T., Ellis, R. S., & Sand, D. J. 2013, *ApJ*, 765, 25
- Ogrean, G. A., van Weeren, R. J., Jones, C., et al. 2015, *ApJ*, 812, 153
- Oke, J. B. 1974, *ApJS*, 27, 21
- Planck Collaboration. 2015, *ArXiv e-prints*, arXiv:1502.01589
- Postman, M., Coe, D., Benítez, N., et al. 2012, *The Astrophysical Journal Supplement*, 199, 25
- Press, W. H. 1997, in *Unsolved Problems in Astrophysics*, ed. J. N. Bahcall & J. P. Ostriker, 49–60
- Richard, J., Jauzac, M., Limousin, M., et al. 2014, *MNRAS*, 444, 268
- Rodney, S. A., Patel, B., Scolnic, D., et al. 2015a, *ArXiv e-prints*, arXiv:1505.06211
- Rodney, S. A., Strolger, L.-G., Kelly, P. L., et al. 2015b, *ArXiv e-prints*, arXiv:1512.05734
- Salpeter, E. E. 1955, *ApJ*, 121, 161
- Sand, D. J., Treu, T., Ellis, R. S., Smith, G. P., & Kneib, J. 2008, *ApJ*, 674, 711
- Schmidt, K. B., Treu, T., Brammer, G. B., et al. 2014, *The Astrophysical Journal Letters*, 782, L36
- Schmidt, K. B., Treu, T., Bradač, M., et al. 2015, *ArXiv e-prints*, arXiv:1511.04205
- Schrabback, T., Erben, T., Simon, P., et al. 2007, *A&A*, 468, 823
- Schrabback, T., Hartlap, J., Joachimi, B., et al. 2010, *A&A*, 516, A63
- Sharon, K., Gladders, M. D., Rigby, J. R., et al. 2014, *ApJ*, 795, 50
- Treu, T., & Ellis, R. S. 2014, *ArXiv e-prints*, arXiv:1412.6916
- Treu, T., Schmidt, K. B., Brammer, G. B., et al. 2015, *ApJ*, 812, 114
- Treu, T., Brammer, G., Diego, J. M., et al. 2016, *ApJ*, 817, 60
- Umetsu, K., Medezinski, E., Nonino, M., et al. 2014, *ApJ*, 795, 163
- Wang, X., Hoag, A., Huang, K.-H., et al. 2015, *ApJ*, 811, 29
- Werner, M. W., Roellig, T. L., Low, F. J., et al. 2004, *ApJS*, 154, 1
- York, D. G., Adelman, J., Anderson, Jr., J. E., et al. 2000, *AJ*, 120, 1579
- Zheng, W., Postman, M., Zitrin, A., et al. 2012, *Nature*, 489, 406
- Zitrin, A., Meneghetti, M., Umetsu, K., et al. 2013, *ApJ*, 762, L30
- Zitrin, A., Zheng, W., Broadhurst, T., et al. 2014, *ApJ*, 793, L12
- Zitrin, A., Fabris, A., Merten, J., et al. 2015, *ApJ*, 801, 44

APPENDIX

A. REDSHIFT PDFS FOR THE SILVER SAMPLE MULTIPLY IMAGED SYSTEMS NOT USED IN THE LENS MODEL

In Figure A1 we show the PDFs of the individual and, where available, combined redshifts of the multiply imaged systems in the Silver sample that we were unable to use in our lens model. We believe these systems are real, but we were unable to sufficiently constrain their redshifts to include them in the lens model.

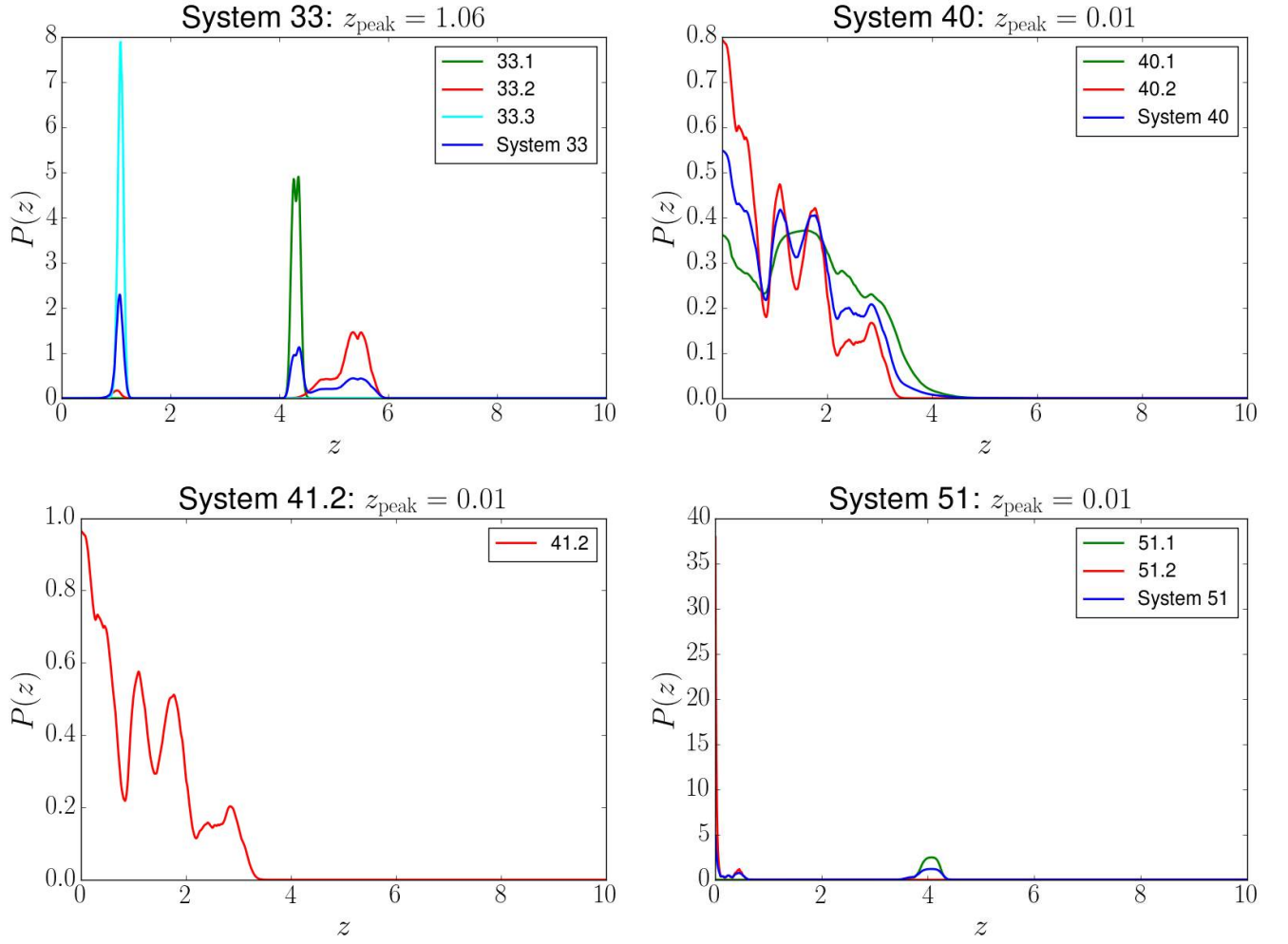


FIG. A1.— Probability density functions (PDFs) for the redshifts of multiple image systems in the Silver sample, which are too poorly constrained to use in the lens model. In all but the bottom left panel, the blue line represents the combined redshift (z_{Bayes}) PDF, derived using the hierarchical Bayesian method developed by Dahlen et al. (2013). In system 41 (bottom left panel), only image 41.2 was detected in the photometric catalog, so multiple redshifts could not be combined. What is shown is the single PDF for the photometric redshift of 41.2, which is very poorly constrained.

B. GLASS SPECTRA OF MULTIPLY IMAGED GALAXIES

In Figures B1-B25 we show the GLASS spectra confirming the redshifts of known multiply imaged galaxies in MACSJ0416.

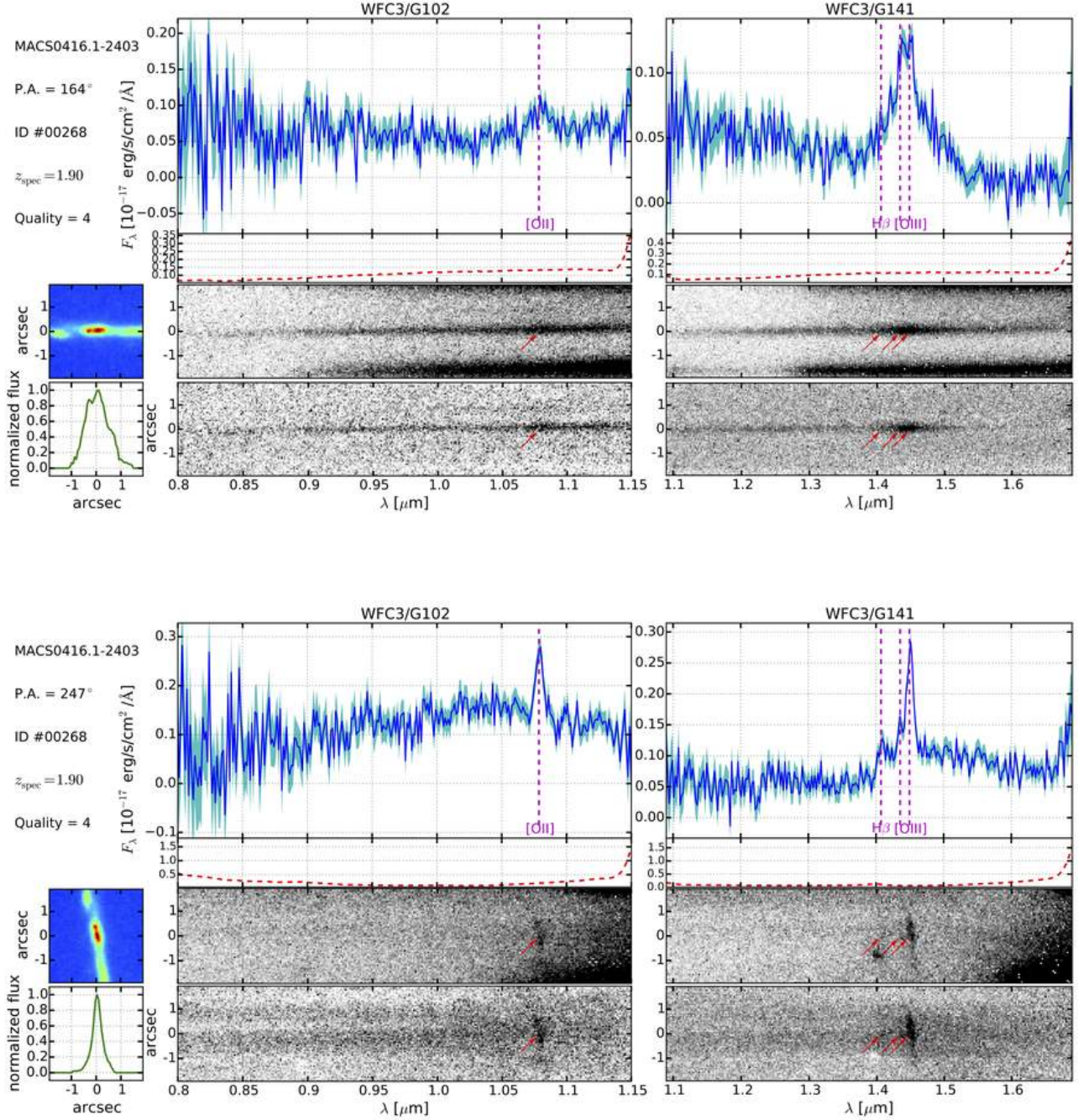


FIG. B1.— Grism spectroscopic confirmation for ID #268 (arc 2.1) observed at the two P.A.s shown in the two sub-figures. In each sub-figure, the two panels on top show the 1-dimensional spectra, where the observed flux and contamination model are denoted by blue solid and red dashed lines respectively. The cyan shaded region represents the noise level. The six panels at the bottom show the 2-dimensional postage stamp created from the coadded HFF+CLASH+GLASS image, the 1-dimensional collapsed image, and the interlaced 2-dimensional spectra without (top) and with (bottom) the contamination subtracted. In the 1- and 2-dimensional spectra, the identified emission lines are denoted by vertical dashed lines in magenta and arrows in red respectively.

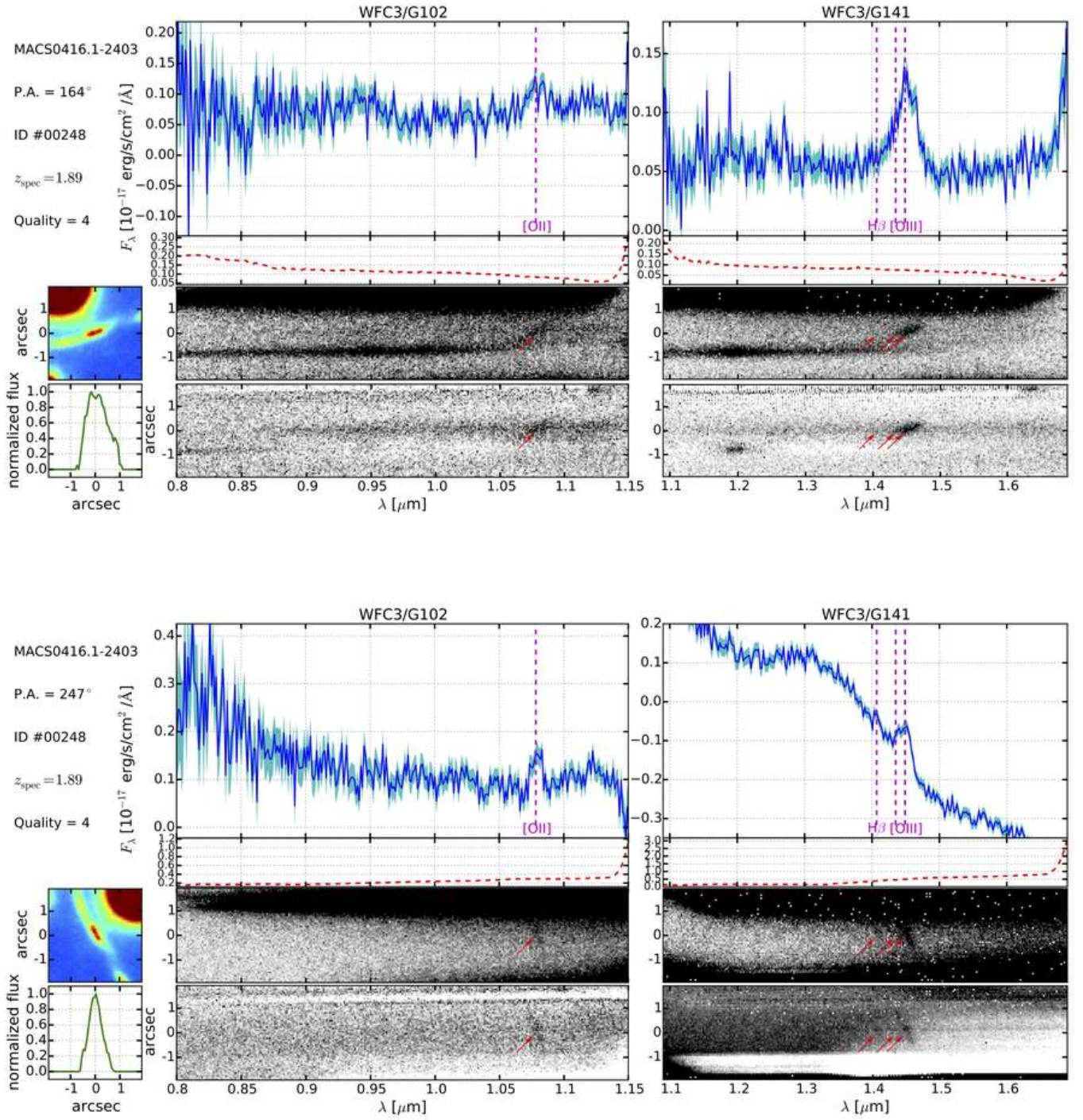


FIG. B2.— Same as Figure B1, except that object ID #248 (arc 2.2) is shown.

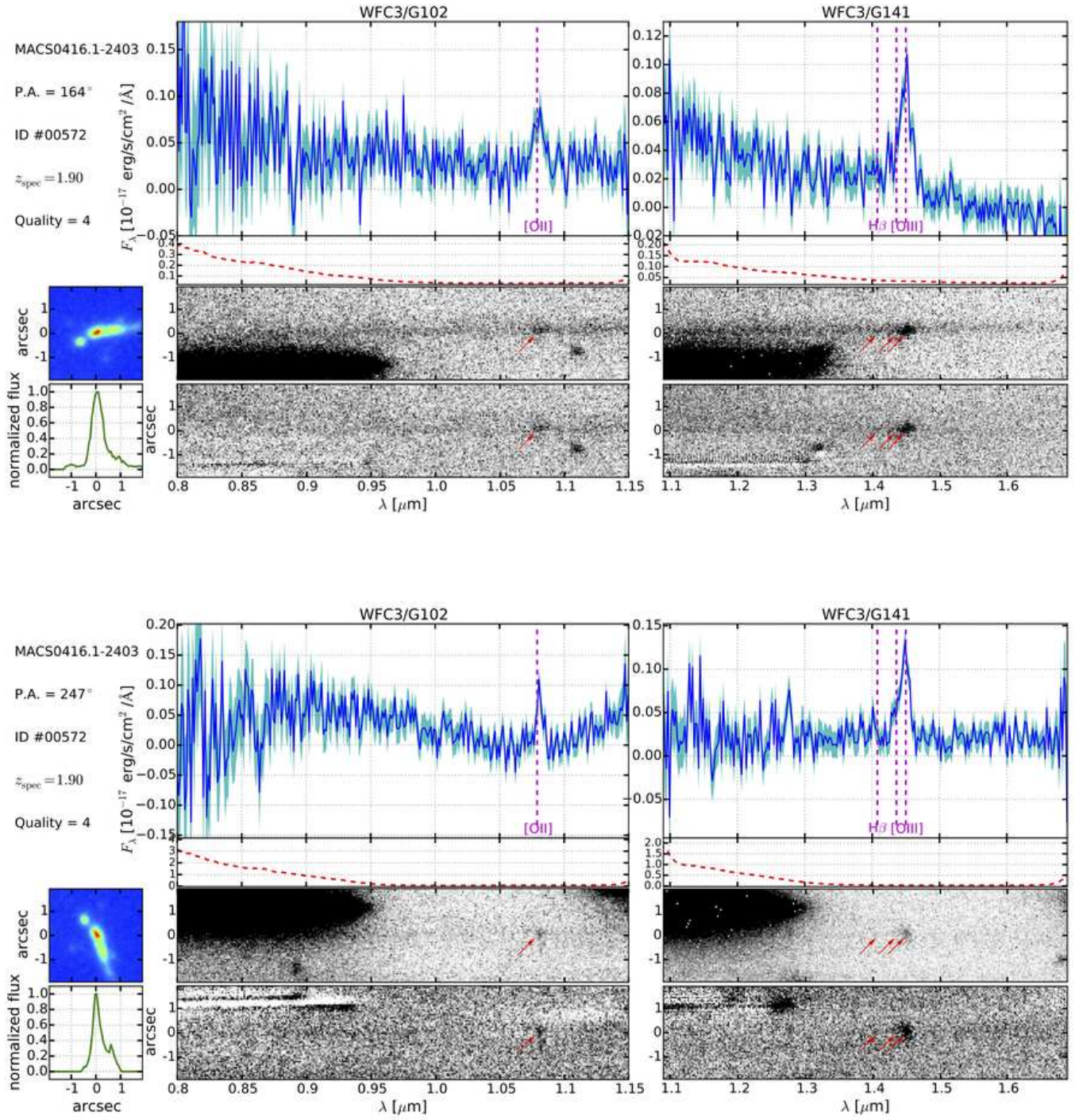
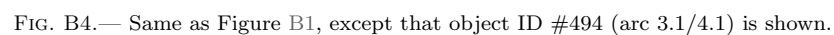


FIG. B3.— Same as Figure B1, except that object ID #572 (arc 2.3) is shown.



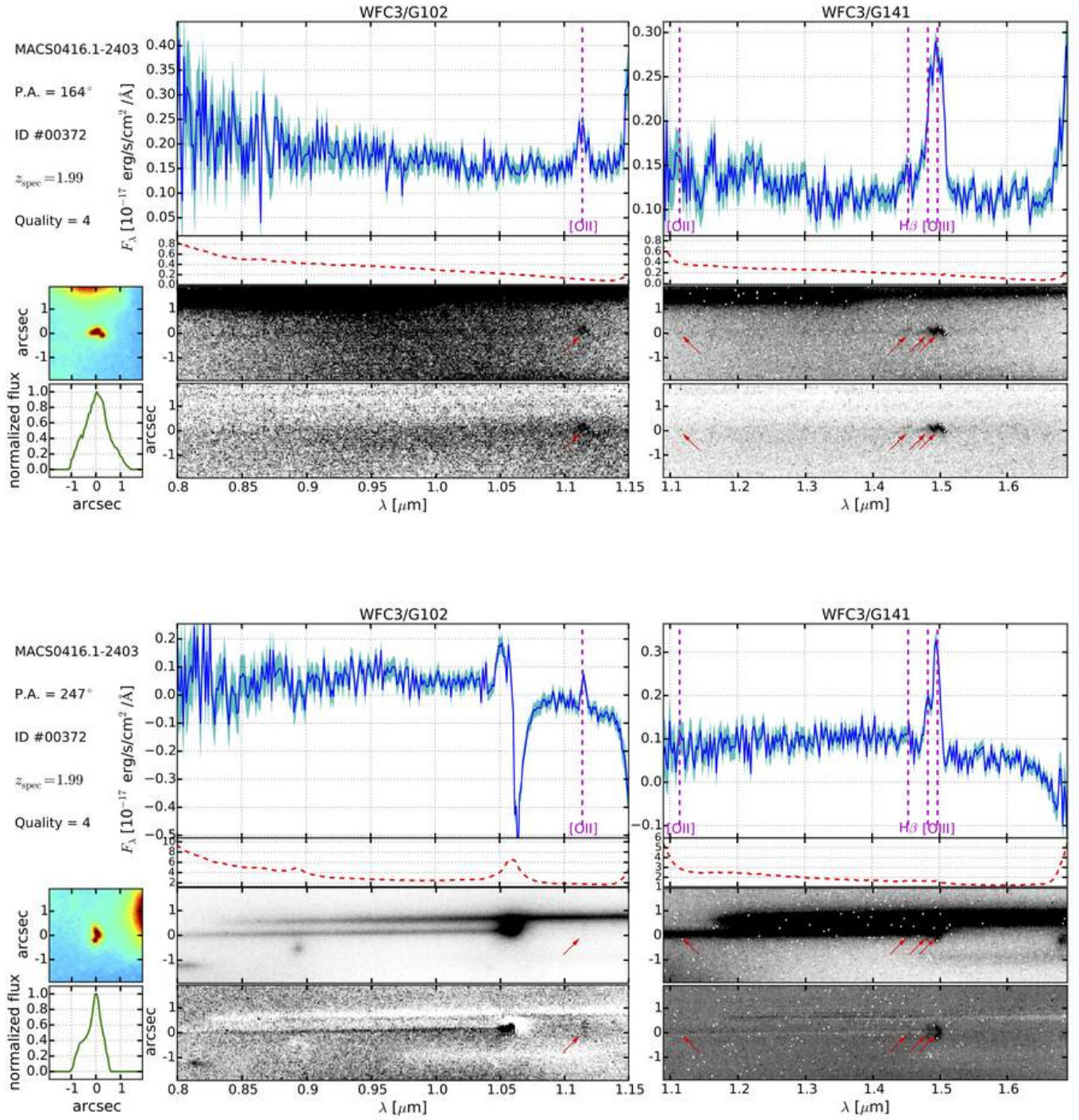
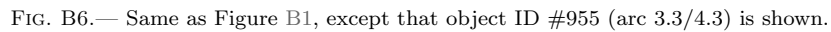


FIG. B5.— Same as Figure B1, except that object ID #372 (arc 3.2/4.2) is shown.



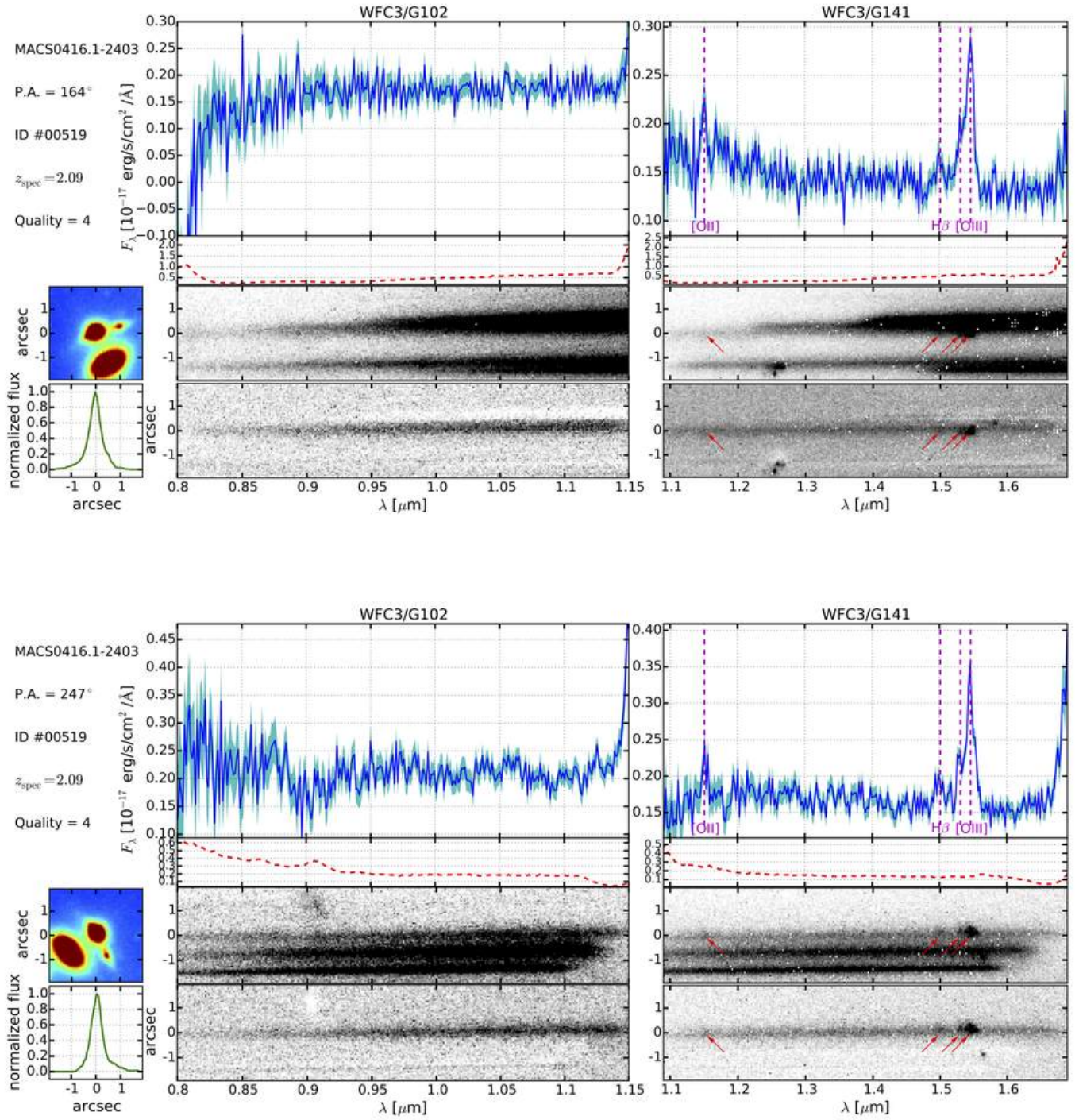


FIG. B7.— Same as Figure B1, except that object ID #519 (arc 5.1) is shown. The multiple image is heavily contaminated by a foreground cluster member, as can be seen in the two-dimensional HFF postage stamp. However, after subtracting the contamination, the emission lines are clearly detected.

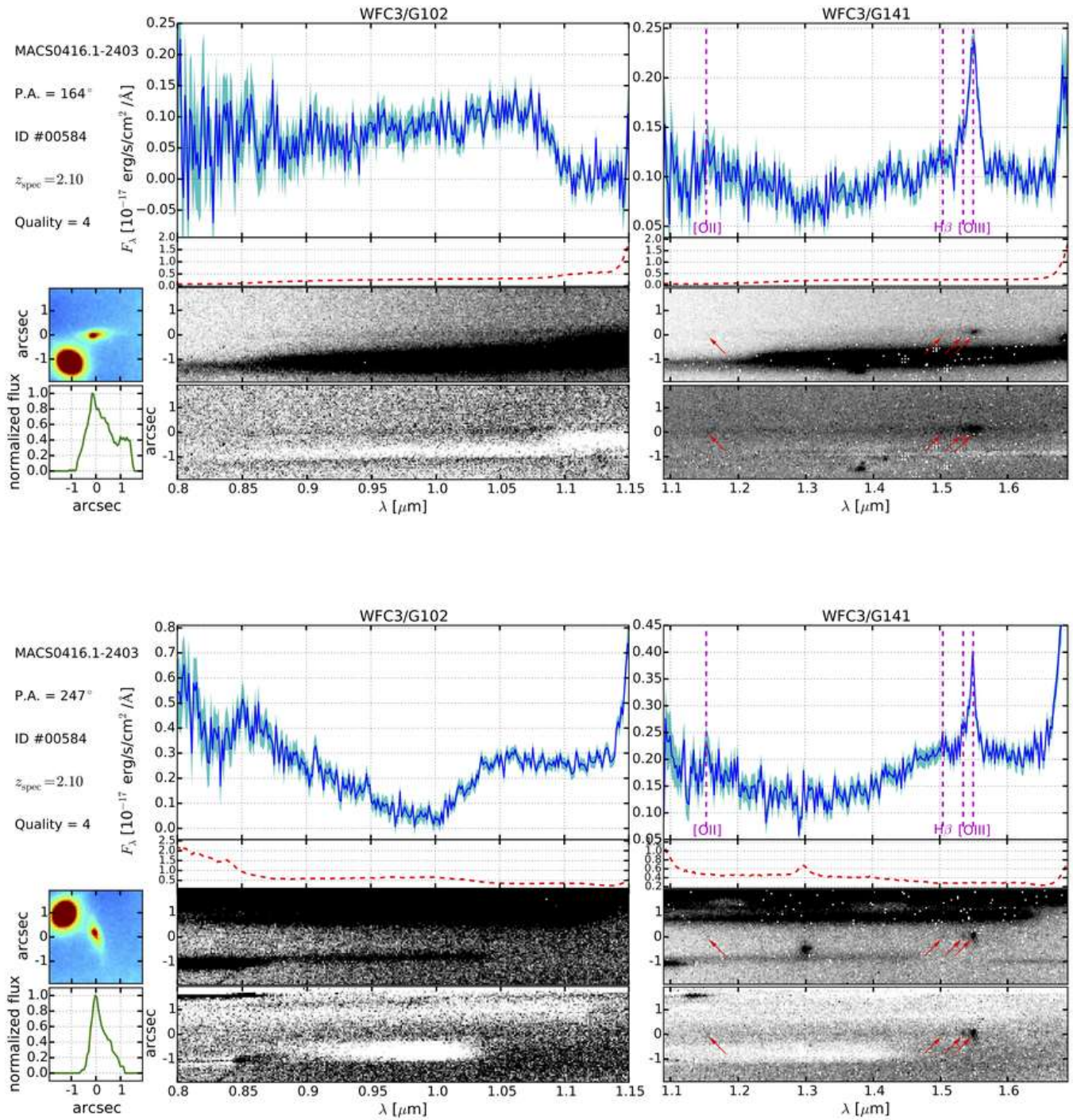


FIG. B9.— Same as Figure B1, except that object ID #584 (arc 5.3) is shown.

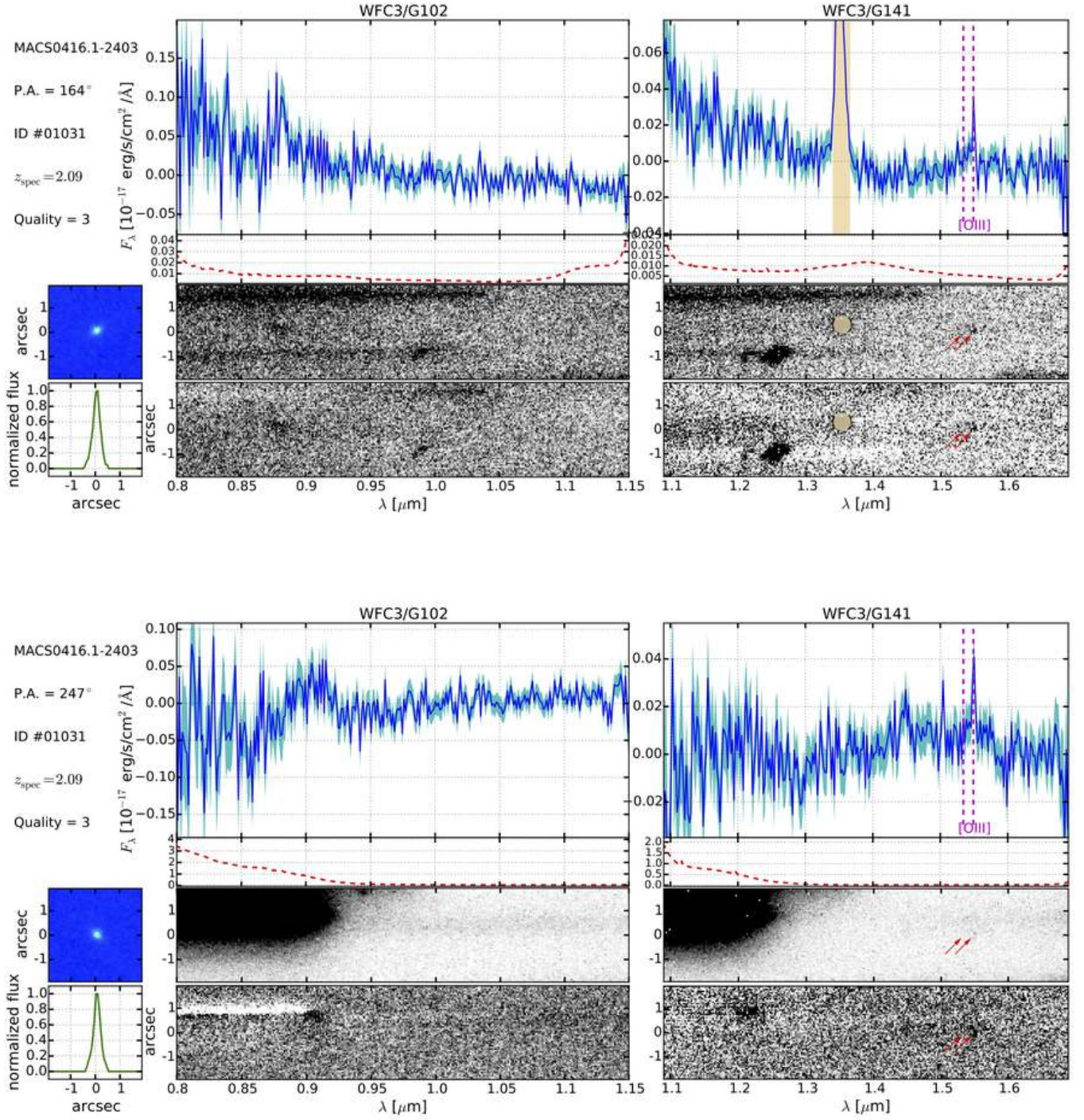


FIG. B10.— Same as Figure B1, except that object ID #1031 (arc 5.4) is shown. The tan colored region in the one- and two-dimensional P.A.=164° G141 spectra covers a contaminant that was not identified by the contamination model.

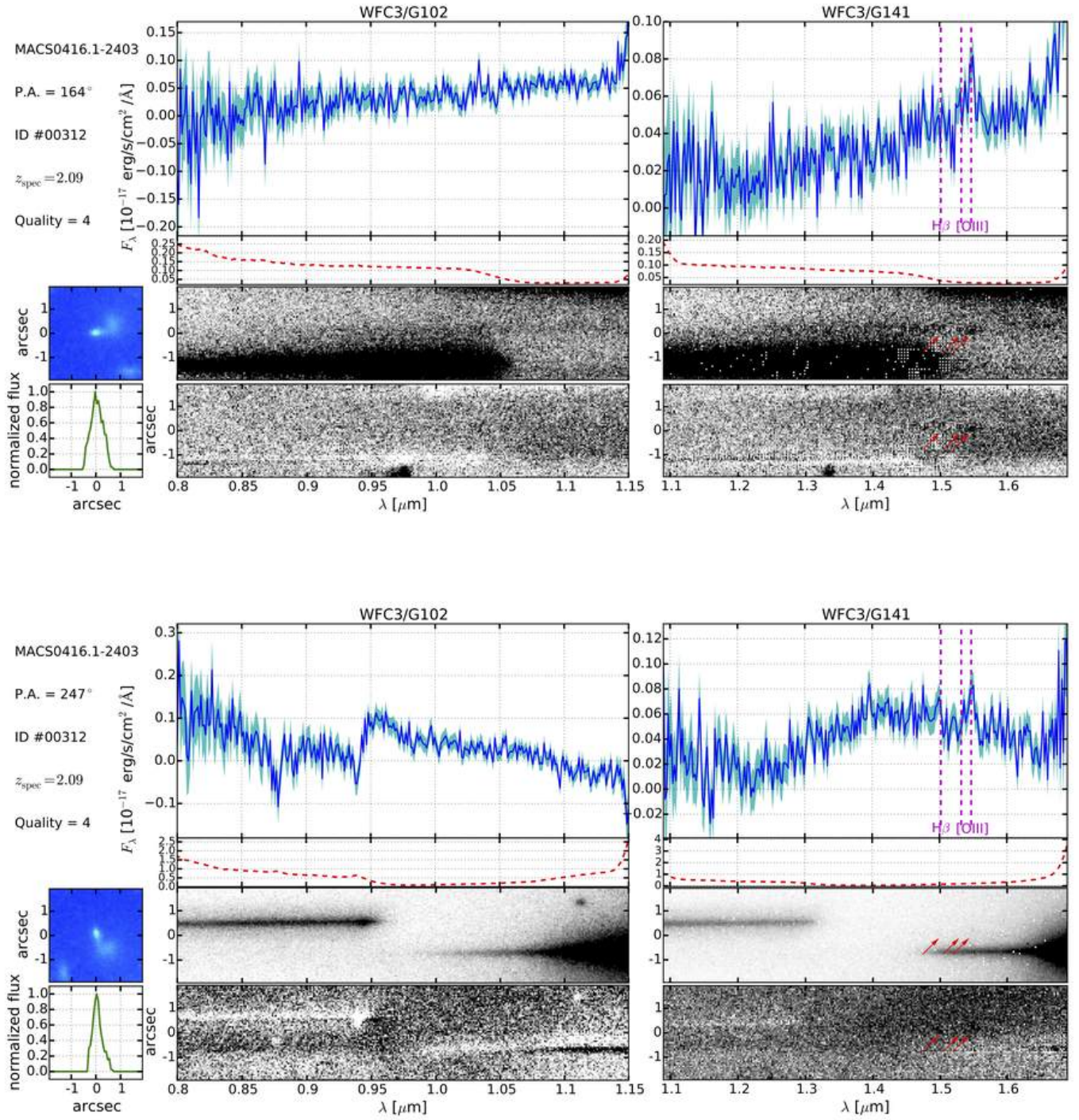


FIG. B11.— Same as Figure B1, except that object ID #312 (arc 7.1) is shown.

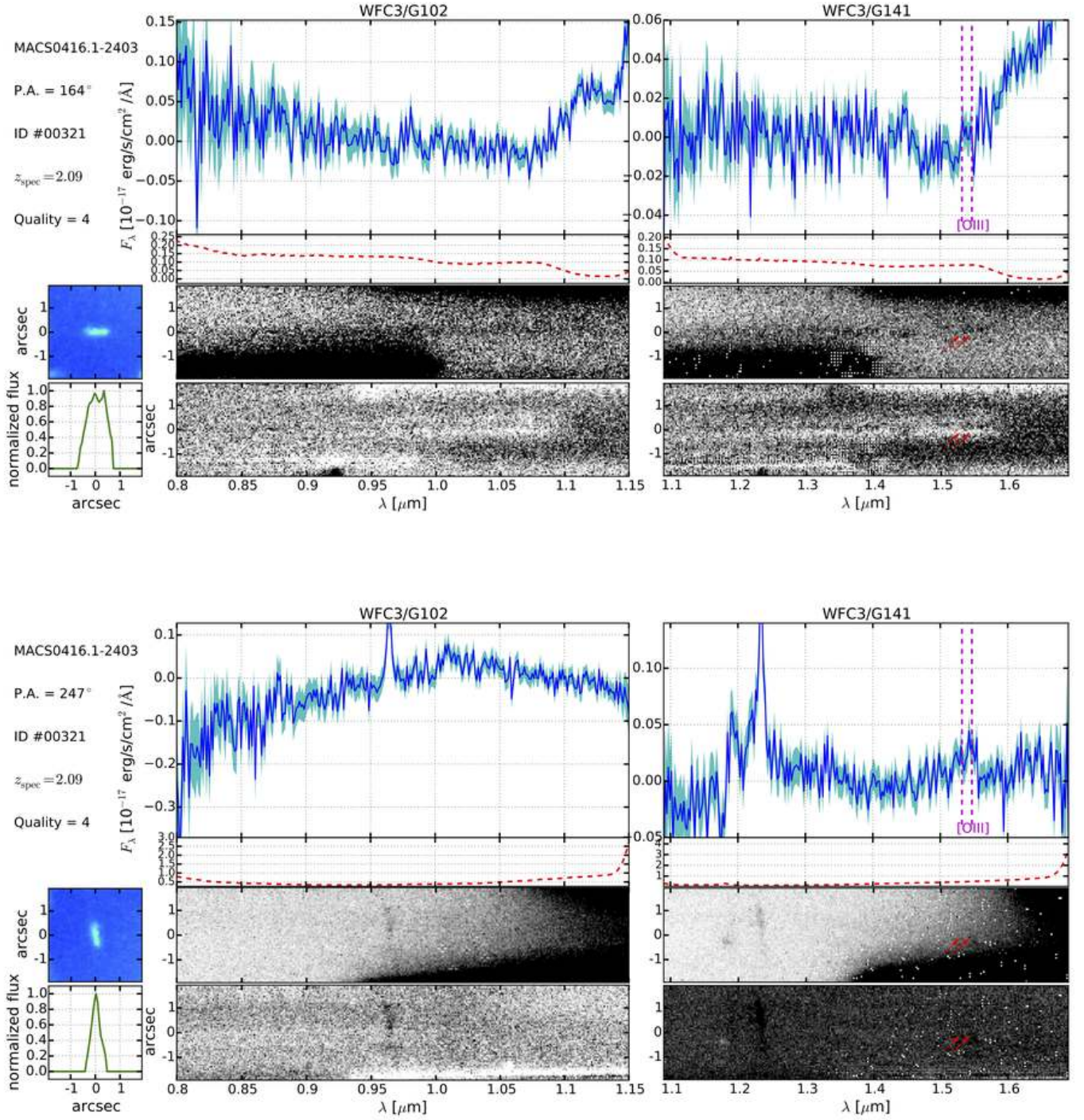


FIG. B12.— Same as Figure B1, except that object ID #321 (arc 7.2) is shown.

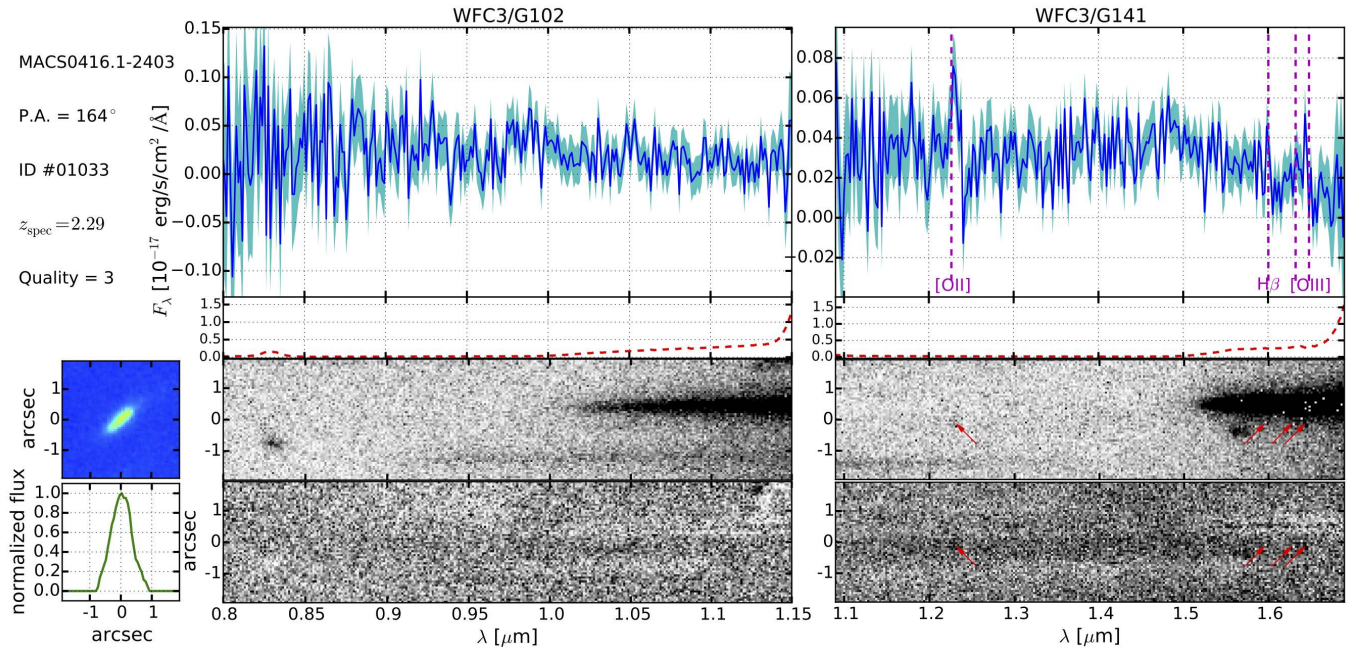


FIG. B13.— Same as Figure B1, except that object ID #1033 (arc 10.1) is shown for a single PA. PA=247 is heavily contaminated, making the identification of emission lines extremely difficult.

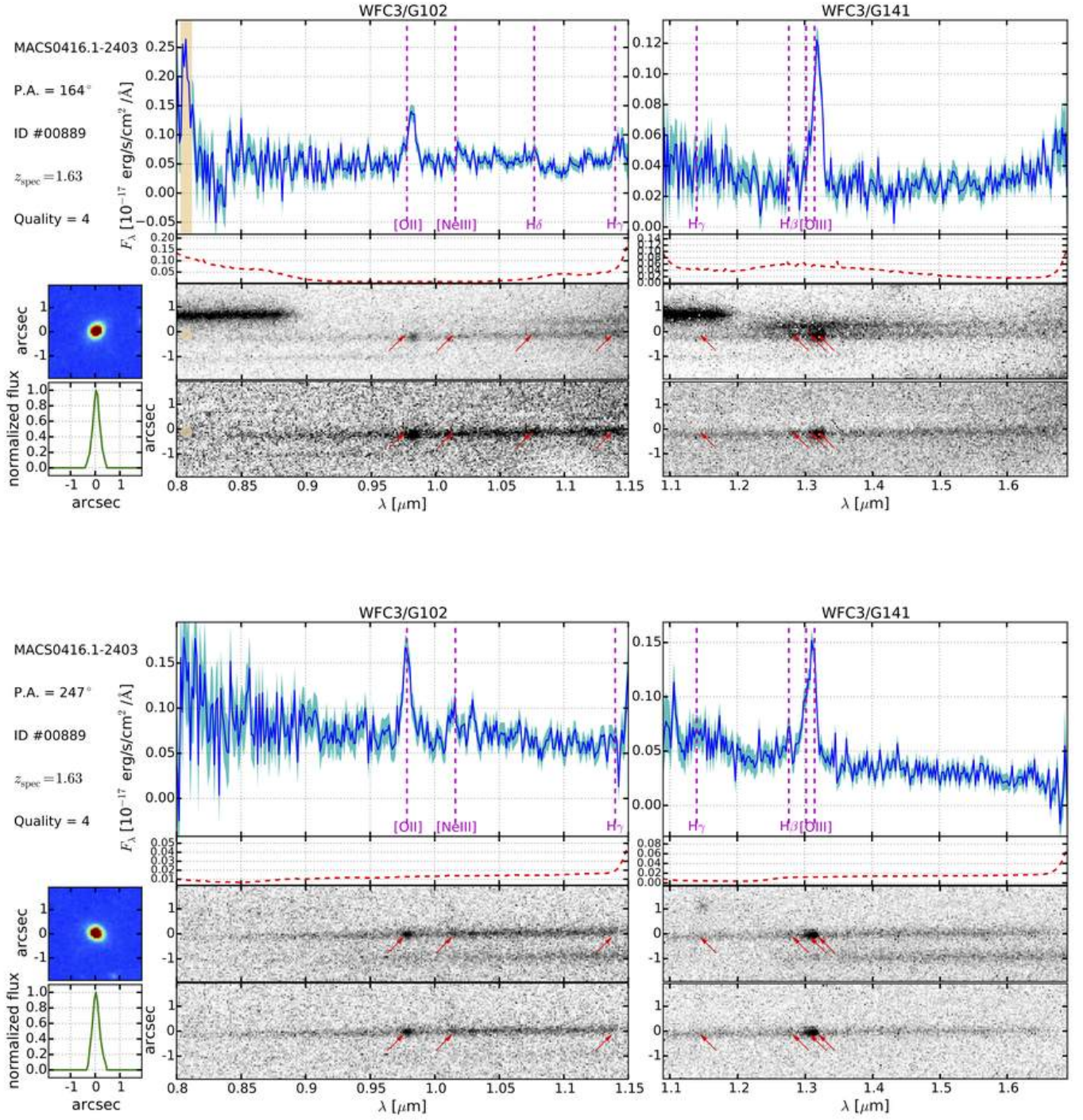


FIG. B14.— Same as Figure B1, except that object ID #889 (arc 14.1) is shown. The tan colored region in the one- and two-dimensional PA=164° G102 spectra covers a contaminant that was not identified by the contamination model.

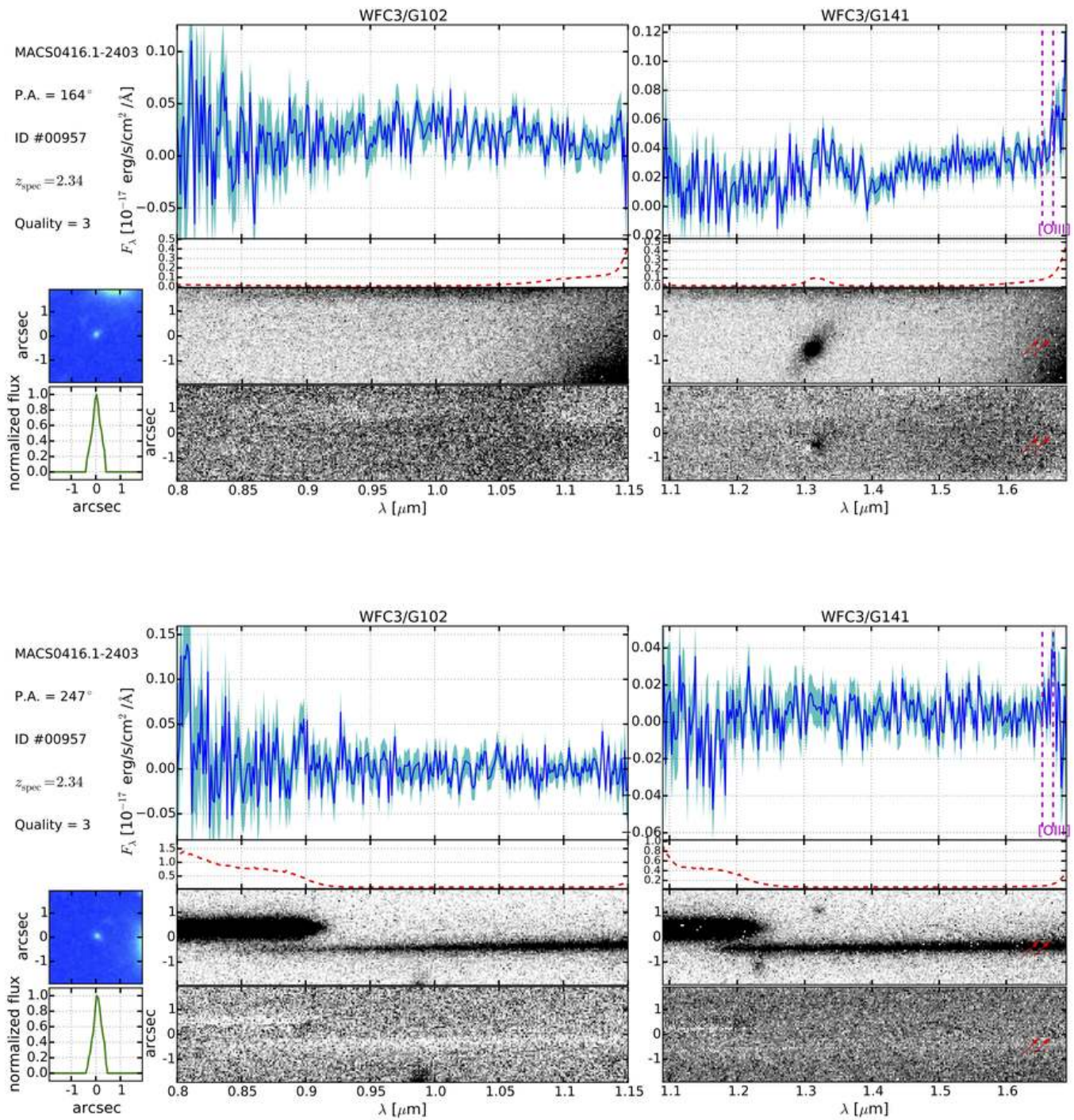


FIG. B17.— Same as Figure B1, except that object ID #957 (arc 15.1) is shown.

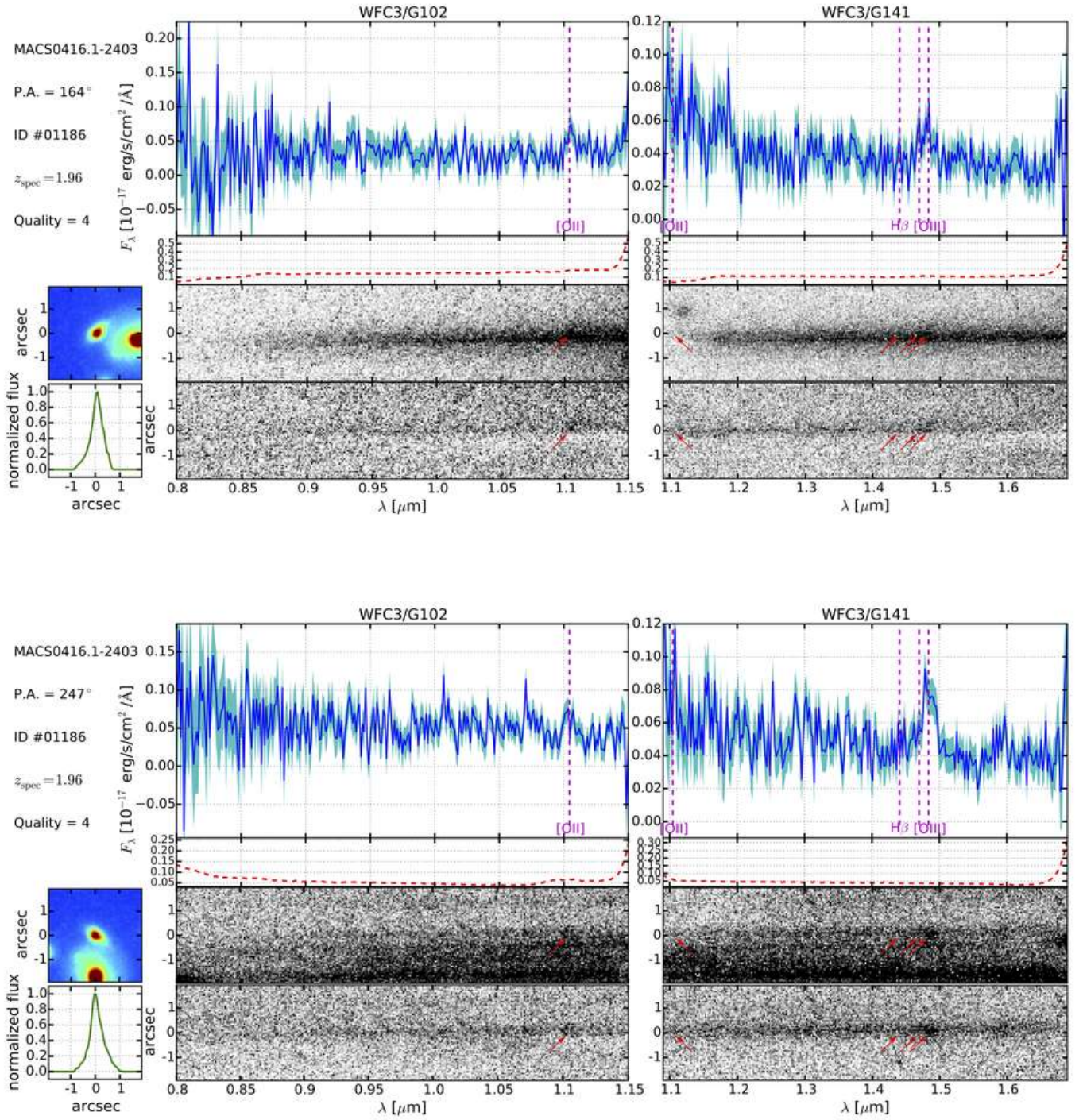
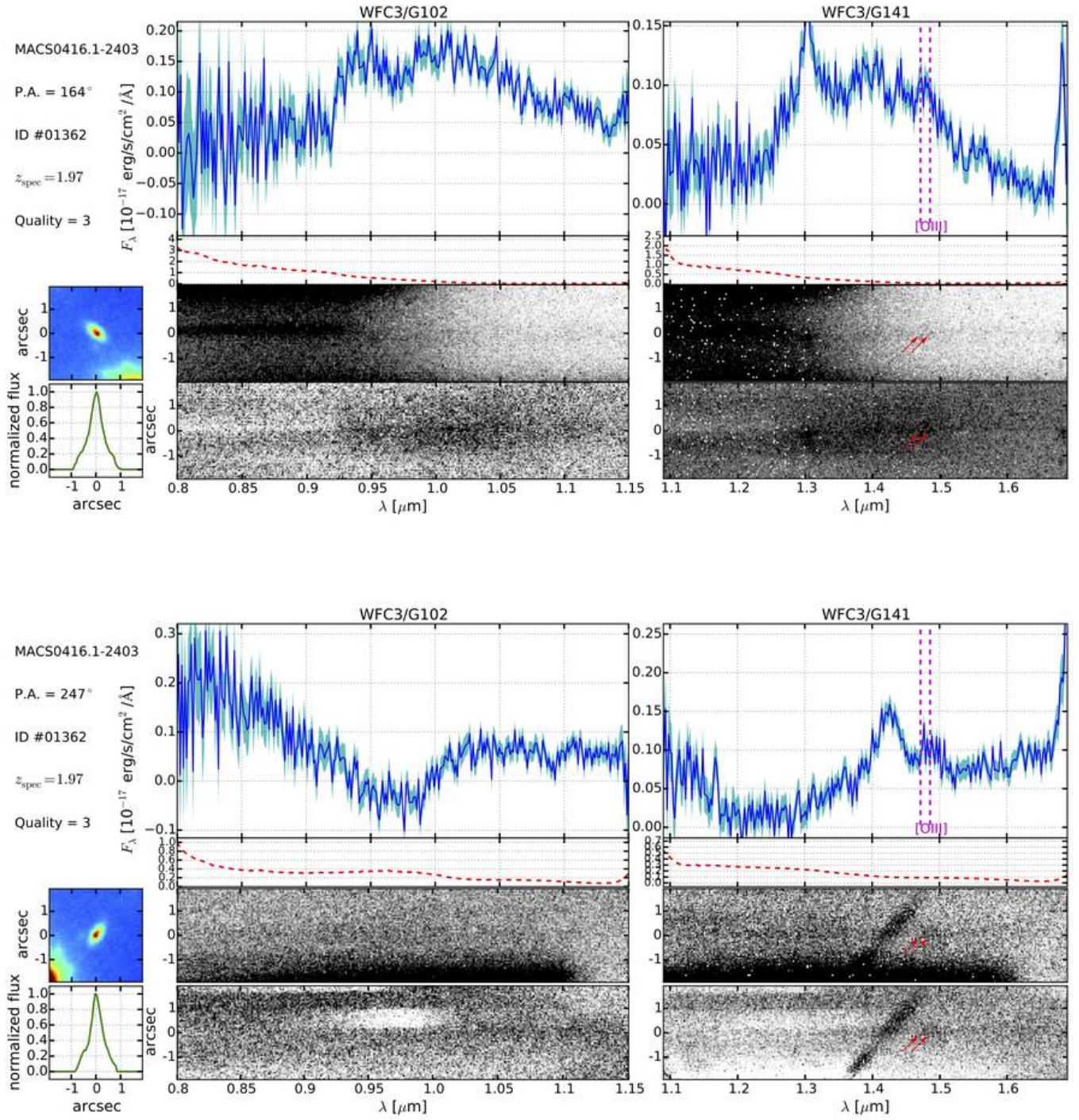


FIG. B18.— Same as Figure B1, except that object ID #1186 (arc 16.1) is shown.



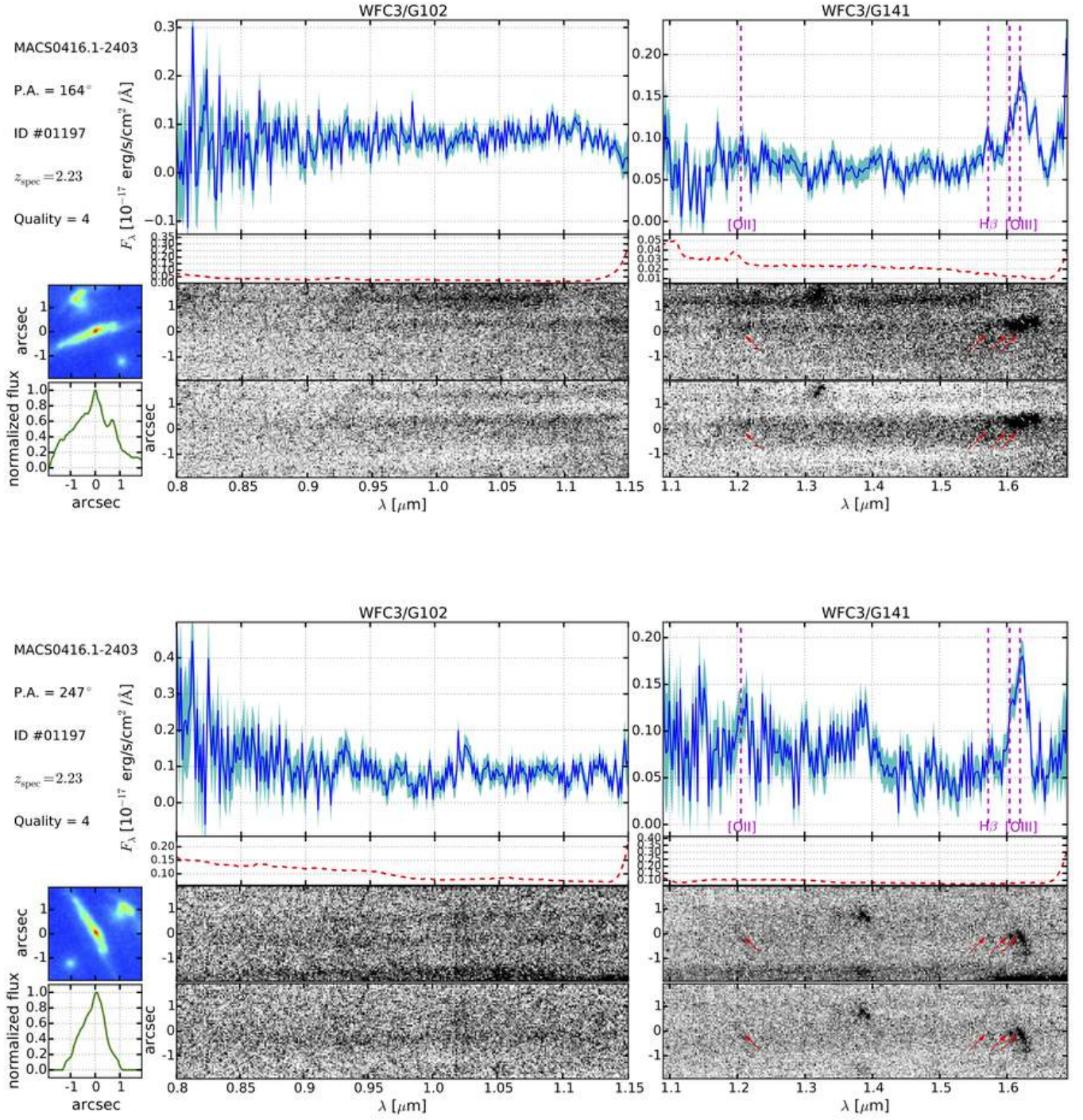


FIG. B20.— Same as Figure B1, except that object ID #1197 (arc 17.3) is shown.

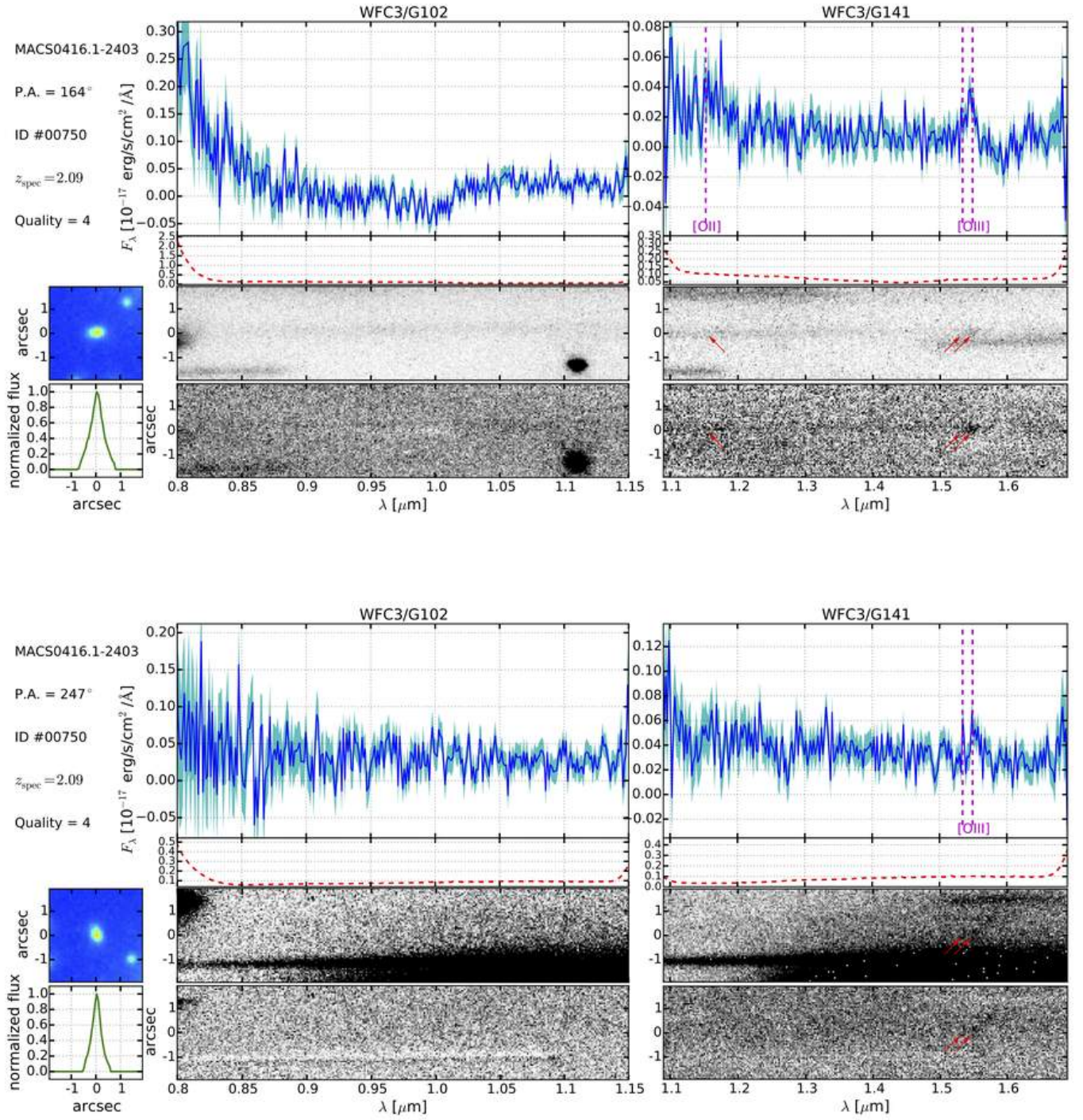


FIG. B21.— Same as Figure B1, except that object ID #750 (arc 23.1) is shown.

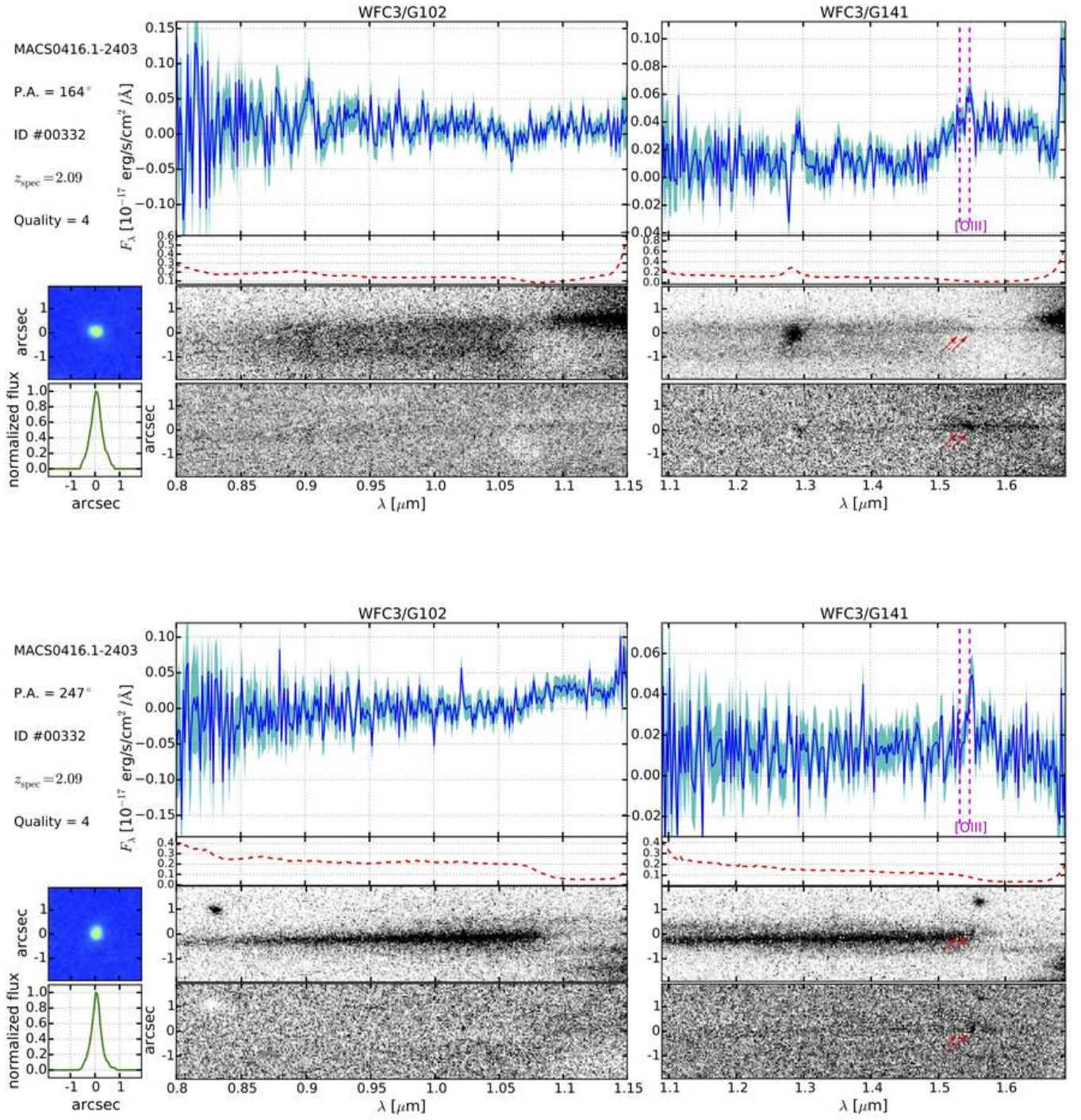
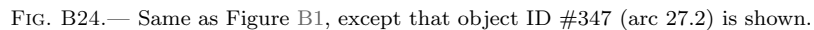


FIG. B22.— Same as Figure B1, except that object ID #332 (arc 23.3) is shown.



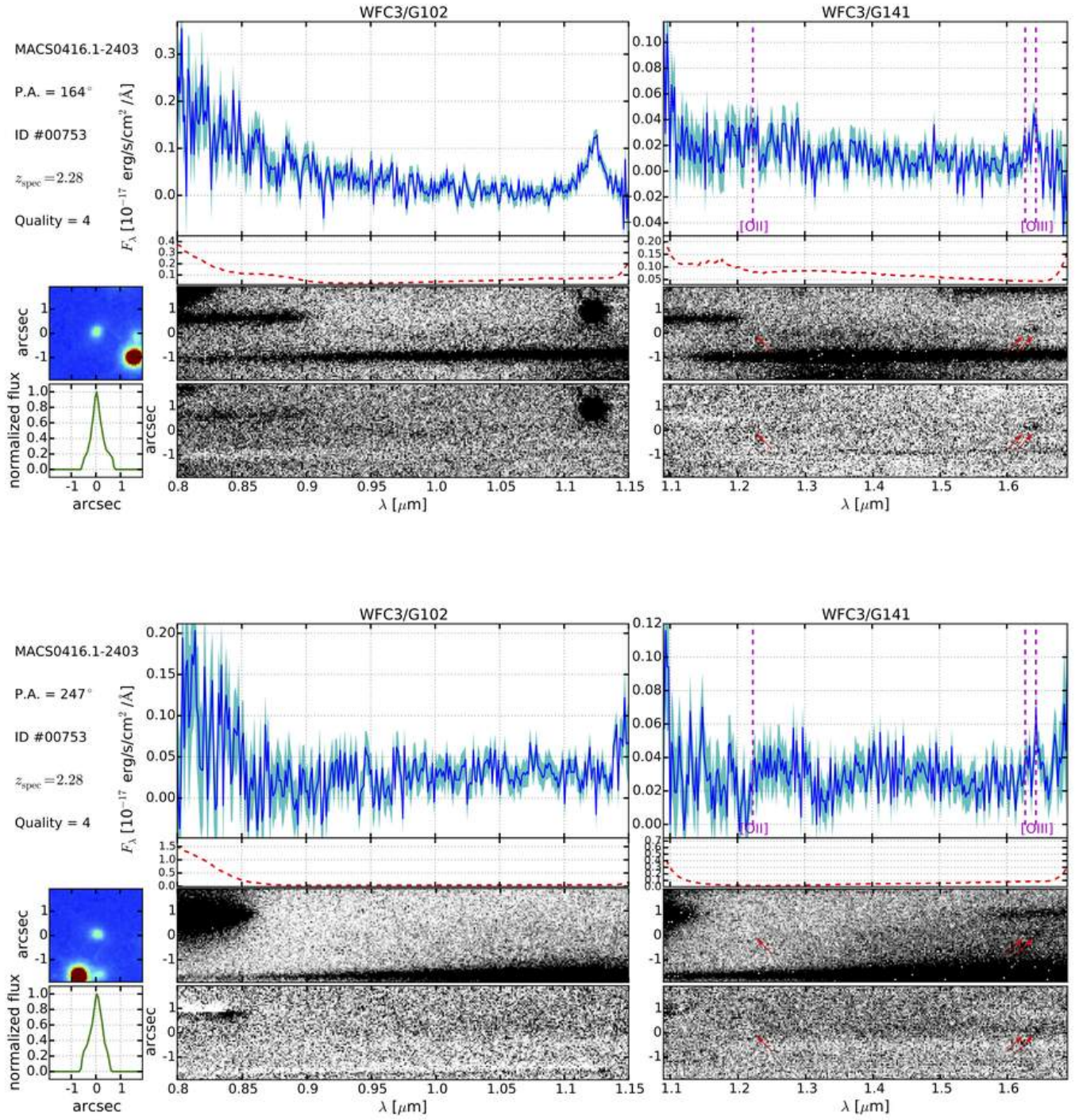


FIG. B25.— Same as Figure B1, except that object ID #753 (arc 29.3) is shown.

TABLE 2
MULTIPLY LENSED ARC SYSTEMS IDENTIFIED IN THE MACSJ0416 FIELD

ID _{arc}	ID _{GLASS}	R.A. (deg.)	Dec. (deg.)	Cref.	z _{spec} (1)	z _{ref} (1)	z _{spec} (2)	z _{ref} (2)	z _{grism}	z _{Bayes}	F140W (mag.)	Magnification ¹	Sample
1.1	245	64.040750	-24.061592	MJ14	1.896	MJ14	1.89	AZ13	...	1.9 ^{+0.1} _{-0.1}	23.92 ± 0.02	5.40 ^{+0.48} _{-0.10}	Gold
1.2	244	64.043479	-24.063542	MJ14	1.896	MJ14	1.896	JR14	23.43 ± 0.02	51.02 ^{+236.36} _{-28.13}	Gold
1.3	571	64.047354	-24.068669	MJ14	1.896	MJ14	1.896	JR14	25.09 ± 0.03	4.03 ^{+0.12} _{-0.04}	Gold
2.1	268	64.041183	-24.061881	MJ14	1.8925	MJ14	1.8925	JR14	1.90	2.4 ^{+0.1} _{-0.2}	23.01 ± 0.01	8.26 ^{+0.97} _{-0.61}	Gold
2.2	248	64.043004	-24.063036	MJ14	1.8925	MJ14	1.8925	JR14	1.89	...	23.08 ± 0.01	8.49 ^{+0.34} _{-0.70}	Gold
2.3	572	64.047475	-24.068850	MJ14	1.8925	MJ14	1.8925	JR14	1.90	...	22.97 ± 0.01	4.13 ^{+0.29} _{-0.37}	Gold
3.1	494	64.030783	-24.067117	MJ14	1.9885	MJ14	1.9885	JR14	1.99	2.5 ^{+0.1} _{-0.3}	23.32 ± 0.01	4.13 ^{+0.03} _{-0.09}	Gold
3.2	372	64.035254	-24.070981	MJ14	1.9885	MJ14	1.9885	JR14	1.99	...	23.13 ± 0.01	2.27 ^{+0.02} _{-0.06}	Gold
3.3	...	64.041817	-24.075711	MJ14	1.9885	MJ14	1.9885	JR14	1.99	3.20 ^{+0.12} _{-0.01}	Gold
4.1 ²	494	64.030825	-24.067225	MJ14	1.9886	1.99	2.4 ^{+0.1} _{-0.2}	23.32 ± 0.01	4.14 ^{+0.17} _{-0.04}	Gold
4.2	372	64.035154	-24.070981	MJ14	1.9887	1.99	...	23.13 ± 0.01	2.39 ^{+0.04} _{-0.07}	Gold
4.3	955	64.041879	-24.075856	MJ14	1.9888	1.99	...	23.21 ± 0.01	3.92 ^{+0.16} _{-0.03}	Gold
5.1 ³	519	64.032375	-24.068411	TJ14	2.09	2.4 ^{+0.1} _{-0.5}	21.58 ± 0.00	14.37 ^{+0.24} _{-1.09}	Bronze
5.2	520	64.032663	-24.068669	MJ14	2.092	IB15	2.09	...	23.78 ± 0.01	25.51 ^{+1.78} _{-1.25}	Gold
5.3	584	64.033513	-24.069447	MJ14	2.10	...	23.14 ± 0.01	4.47 ^{+0.24} _{-0.08}	Gold
5.4 ³	1031	64.043554	-24.076951	JKP	2.09	...	25.56 ± 0.05	2.55 ^{+0.00} _{-0.03}	...
6.1	258	64.040042	-24.061839	TJ14	26.75 ± 0.14
6.2	...	64.041458	-24.062589	TJ14
6.3	...	64.049400	-24.072235	RK
7.1	312	64.039800	-24.063092	MJ14	2.0854	MJ14	2.0854	JR14	2.09	2.4 ^{+0.4} _{-0.3}	24.89 ± 0.04	401.21 ^{+130.09} _{-310.13}	Gold
7.2	321	64.040633	-24.063561	MJ14	2.0854	MJ14	2.0854	JR14	2.09	...	24.95 ± 0.03	14.51 ^{+0.36} _{-2.02}	Gold
7.3	700	64.047117	-24.071108	MJ14	2.0854	MJ14	2.0854	JR14	27.59 ± 0.17	2.80 ^{+0.02} _{-0.03}	Gold
8.1	432	64.036596	-24.066125	MJ14	Silver
8.2	433	64.036833	-24.066342	MJ14	Silver
8.3p	924	64.046070	-24.075174	JKP	27.12 ± 0.13
9.1	1088	64.027025	-24.078583	MJ14	2.3 ^{+0.1} _{-0.2}	24.84 ± 0.04	66.68 ^{+198.44} _{-16.13}	Silver
9.2	1107	64.027521	-24.079106	MJ14	24.51 ± 0.04	19.27 ^{+14.36} _{-1.15}	Silver
9.3	...	64.036453	-24.083973	MJ14	27.62 ± 0.16	3.45 ^{+0.13} _{-0.03}	...
10.1	1033	64.026017	-24.077156	MJ14	2.2982	MJ14	2.2982	JR14	2.29	2.5 ^{+0.3} _{-0.1}	23.96 ± 0.02	8.47 ^{+0.11} _{-0.73}	Gold
10.2	1144	64.028471	-24.079756	MJ14	2.2982	MJ14	2.2982	JR14	24.44 ± 0.02	6.23 ^{+0.20} _{-0.56}	Gold
10.3	1326	64.036692	-24.083901	MJ14	2.2982	MJ14	2.2982	JR14	25.00 ± 0.03	3.23 ^{+0.20} _{-0.05}	Gold
11.1	...	64.039208	-24.070367	MJ14	1.0054	SR14	7.09 ^{+0.12} _{-0.15}	Gold
11.2	...	64.038317	-24.069753	MJ14	1.0054	SR14	64.80 ^{+15.53} _{-21.45}	Gold
11.3	440	64.034259	-24.066018	MJ14	26.37 ± 0.08	3.15 ^{+0.01} _{-0.10}	...
11.3a	471	64.035807	-24.066659	24.80 ± 0.03	7.10 ^{+0.25} _{-0.84}	...
12.1	734	64.038263	-24.073696	MJ14	2.0 ^{+0.2} _{-1.4}	23.48 ± 0.02	20.05 ^{+18.15} _{-0.89}	Silver
12.2	736	64.037686	-24.073294	MJ14	23.43 ± 0.01	40.51 ^{+9.46} _{-20.56}	Silver
12.3 ⁴	...	64.029117	-24.066742	MJ14	1.95	2.84 ^{+0.11} _{-0.00}	...
13.1	784	64.027579	-24.072786	MJ14	3.2226	MJ14	3.2226	JR14	...	3.4 ^{+0.1} _{-0.1}	24.68 ± 0.03	6.90 ^{+0.03} _{-0.32}	Gold
13.2	...	64.032129	-24.075169	MJ14	3.2226	MJ14	3.2226	JR14	2.72 ^{+0.06} _{-0.20}	Gold
13.3	1224	64.040338	-24.081544	MJ14	3.2226	MJ14	3.2226	JR14	26.10 ± 0.07	2.88 ^{+0.02} _{-0.02}	Gold
14.1 ⁵	889	64.026233	-24.074339	MJ14	2.0531	JR14	1.637	CG15	1.63	1.8 ^{+0.1} _{-0.2}	22.97 ± 0.01	4.58 ^{+0.09} _{-0.29}	Gold
14.2	880	64.031042	-24.078961	MJ14	2.0531	JR14	1.637	CG15	1.63	...	22.92 ± 0.01	2.16 ^{+0.09} _{-0.15}	Gold
14.3	1213	64.035825	-24.081328	MJ14	2.0531	JR14	1.63	...	22.74 ± 0.01	4.78 ^{+0.05} _{-0.29}	Gold
15.1	957	64.026860	-24.075745	MJ14	2.34	3.2 ^{+0.1} _{-0.5}	26.16 ± 0.07	15.01 ^{+0.43} _{-2.52}	Gold
15.2	...	64.029438	-24.078583	MJ14	25.96 ± 0.06	4.04 ^{+0.00} _{-0.53}	Bronze
15.3	...	64.038217	-24.082993	MJ14	3.65 ^{+0.17} _{-0.22}	...
16.1	1186	64.024058	-24.080894	MJ14	1.9644	MJ14	1.96	2.9 ^{+5.2} _{-2.1}	...	5.23 ^{+0.16} _{-0.10}	Gold
16.2	...	64.028329	-24.084542	MJ14	1.9644	MJ14	22.79 ± 0.01	5.58 ^{+0.25} _{-0.14}	Gold
16.3	1362	64.031596	-24.085769	MJ14	1.9644	CG15	1.97	...	23.65 ± 0.01	6.05 ^{+0.30} _{-0.27}	Gold
17.1	...	64.029875	-24.086364	MJ14	2.2181	MJ14	2.2181	JR14	38.61 ^{+0.59} _{-23.24}	Gold
17.2	...	64.028608	-24.085986	MJ14	2.2181	MJ14	2.2181	JR14	11.05 ^{+1.14} _{-1.15}	Gold
17.3	1197	64.023329	-24.081581	MJ14	2.2181	MJ14	2.2181	JR14	2.23	4.27 ^{+0.05} _{-0.04}	Gold
18.1	1341	64.026075	-24.084233	MJ14	26.06 ± 0.09	...	Silver
18.2	1305	64.025067	-24.083350	MJ14	Silver
18.3	...	64.030900	-24.086744	MJ14
23.1	750	64.044546	-24.072100	MJ14	2.09	2.4 ^{+0.4} _{-0.2}	24.22 ± 0.02	3.06 ^{+0.03} _{-0.03}	Gold
23.2	752	64.039604	-24.066631	MJ14	24.57 ± 0.03	1.75 ^{+0.04} _{-0.22}	Gold
23.3	332	64.034342	-24.063742	MJ14	2.09	...	24.40 ± 0.02	4.09 ^{+0.03} _{-0.08}	Gold

TABLE 2 — *Continued*

ID _{arc}	ID _{GLASS}	R.A. (deg.)	Dec. (deg.)	Cref.	$z_{\text{spec}}(1)$	$z_{\text{ref}}(1)$	$z_{\text{spec}}(2)$	$z_{\text{ref}}(2)$	z_{grism}	z_{Bayes}	F140W (mag.)	Magnification ¹	Sample
24.1	301	64.040915	-24.062959	MJ14	$2.4^{+0.4}_{-0.2}$	25.36 ± 0.05	$16.03^{+0.65}_{-2.78}$	Bronze
24.2	302	64.041066	-24.063057	MJ14	25.72 ± 0.05	$10.90^{+0.30}_{-1.43}$	Bronze
24.3	676	64.048893	-24.070871	MJ14	26.73 ± 0.11	$2.44^{+0.04}_{-0.04}$...
24.3a	...	64.047590	-24.070764	JPk	27.79 ± 0.22	$2.80^{+0.02}_{-0.04}$...
25.1	...	64.044891	-24.061068	MJ14	$2.4^{+0.1}_{-0.1}$	25.42 ± 0.08	$28.95^{+5.52}_{-4.74}$	Bronze
25.2	...	64.045448	-24.061409	MJ14	26.15 ± 0.09	$120.48^{+68.55}_{-44.83}$	Bronze
25.3	...	64.048254	-24.064513	MJ14	$13.31^{+1.78}_{-0.37}$	Bronze
25.4	479	64.049697	-24.066948	MJ14	25.13 ± 0.05	$3.61^{+0.05}_{-0.20}$	Bronze
26.1	209	64.046470	-24.060393	MJ14	2.19	$3.4^{+0.2}_{-0.2}$	26.70 ± 0.15	$14.66^{+0.30}_{-3.24}$	Gold
26.2	217	64.046963	-24.060793	MJ14	27.43 ± 0.18	$8.16^{+0.33}_{-0.45}$	Bronze
26.3	...	64.049089	-24.062876	MJ14	27.85 ± 0.22	$6.00^{+0.73}_{-0.18}$...
27.1	488	64.048159	-24.066959	MJ14	25.14 ± 0.04	$129.11^{+484.48}_{-31.29}$	Silver
27.2	347	64.047465	-24.066026	MJ14	2.11	...	23.49 ± 0.02	$69.69^{+17.58}_{-2.07}$	Gold
27.3	210	64.042226	-24.060543	MJ14	25.15 ± 0.05	$5.63^{+0.43}_{-0.09}$	Bronze
28.1	...	64.036457	-24.067026	MJ14	0.94	$65.86^{+57.83}_{-11.08}$	Gold
28.2	...	64.036870	-24.067498	MJ14	0.94	$10.14^{+2.65}_{-0.85}$	Gold
28.3	...	64.040923	-24.071151	MJ14	$2.95^{+0.09}_{-0.01}$...
28.3a ⁶	788	64.044083	-24.074456	D15	0.7097	IB15	20.28 ± 0.00	$1.99^{+0.03}_{-0.03}$...
29.1 ⁷	280	64.034272	-24.063032	MJ14	$2.4^{+0.1}_{-0.4}$	24.56 ± 0.03	$3.61^{+0.00}_{-0.08}$	Gold
29.2	...	64.040131	-24.066757	MJ14	25.12 ± 0.06	$1.56^{+0.04}_{-0.05}$...
29.2a ⁶	428	64.040480	-24.066330	RK	2.2669	IB15	$1.17^{+0.07}_{-0.01}$...
29.3	753	64.044610	-24.071482	MJ14	2.28	...	24.56 ± 0.03	$3.40^{+0.04}_{-0.05}$	Gold
30.1	1248	64.033088	-24.081806	MJ14	$2.7^{+0.2}_{-0.2}$	25.73 ± 0.09	$85.52^{+15.90}_{-66.51}$	Silver
30.2	1240	64.032649	-24.081546	MJ14	25.75 ± 0.07	$10.00^{+6.82}_{-0.76}$	Silver
31.1	1061	64.023833	-24.077621	MJ14	$2.0^{+0.7}_{-0.3}$	25.60 ± 0.05	$4.27^{+0.68}_{-0.02}$	Silver
31.2	...	64.030507	-24.082725	MJ14	24.89 ± 0.06	$4.37^{+0.26}_{-0.06}$	Silver
31.3	1335	64.032456	-24.083821	MJ14	24.88 ± 0.04	$9.37^{+1.05}_{-1.50}$	Silver
32.1	1241	64.024130	-24.081640	MJ14						

TABLE 2 — *Continued*

ID _{arc}	ID _{GLASS}	R.A. (deg.)	Dec. (deg.)	Cref.	$z_{\text{spec}}(1)$	$z_{\text{ref}}(1)$	$z_{\text{spec}}(2)$	$z_{\text{ref}}(2)$	z_{grism}	z_{Bayes}	F140W (mag.)	Magnification ¹	Sample
42.1	674	64.045994	-24.070768	MJ14	26.65 ± 0.11	$3.48^{+0.07}_{-0.11}$	Bronze
42.2	...	64.042073	-24.065547	MJ14	24.97 ± 0.06	$2.77^{+0.02}_{-0.08}$	Bronze
42.3	261	64.035786	-24.061938	MJ14	27.02 ± 0.13	$2.69^{+0.18}_{-0.07}$	Bronze
43.1	1253	64.035667	-24.082050	MJ14	27.00 ± 0.12	$6.06^{+0.18}_{-1.10}$	Silver
43.2	1191	64.031195	-24.079959	MJ14	26.49 ± 0.12	$1.89^{+0.02}_{-0.12}$	Silver
43.3	...	64.024425	-24.073603	MJ14	$4.58^{+0.04}_{-0.34}$	Bronze
44.1	...	64.045259	-24.062757	MJ14	$3.5^{+0.1}_{-0.1}$	25.26 ± 0.05	$10.11^{+0.39}_{-0.36}$	Bronze
44.2	185	64.041543	-24.059997	MJ14	25.66 ± 0.06	$5.87^{+0.13}_{-0.05}$	Bronze
44.3	...	64.049237	-24.068168	MJ14	27.68 ± 0.18	$3.36^{+0.02}_{-0.11}$...
45.1 ⁶	1159	64.035673	-24.079918	MJ14	2.545	IB15	$2.2^{+0.3}_{-2.1}$	25.92 ± 0.06	$9.21^{+0.17}_{-1.52}$...
45.1a	...	64.037646	-24.080469	JKP	26.78 ± 0.11	$4.86^{+0.29}_{-0.35}$...
45.2	...	64.025766	-24.072231	MJ14	24.06 ± 0.03	$5.09^{+0.08}_{-0.55}$...
45.3	...	64.032893	-24.076993	MJ14	$10.96^{+5.54}_{-4.63}$...
46.1	...	64.038256	-24.080451	MJ14	$2.4^{+0.5}_{-2.1}$	27.88 ± 0.20	$4.09^{+0.18}_{-0.30}$	Bronze
46.2	...	64.026402	-24.072239	MJ14	27.70 ± 0.20	$5.79^{+0.15}_{-0.49}$	Bronze
46.3	...	64.033057	-24.076204	MJ14	$2.49^{+0.15}_{-0.07}$	Bronze
47.1	...	64.026328	-24.076694	MJ14	$3.4^{+0.2}_{-1.0}$	25.92 ± 0.08	$14.56^{+0.14}_{-3.84}$	Bronze
47.2	...	64.028329	-24.078999	MJ14	$6.23^{+0.47}_{-0.25}$	Bronze
47.3	1320	64.038206	-24.083719	MJ14	26.14 ± 0.08	$4.30^{+0.44}_{-0.07}$...
48.1	1376	64.035489	-24.084668	MJ14	$4.1^{+0.3}_{-3.7}$	26.31 ± 0.08	$4.22^{+0.06}_{-0.86}$	Silver
48.2	...	64.029244	-24.081802	MJ14	24.06 ± 0.03	$3.53^{+1.33}_{-0.08}$	Silver
48.3	977	64.023416	-24.076122	MJ14	25.16 ± 0.05	$4.86^{+0.32}_{-0.15}$	Silver
49.1	896	64.033944	-24.074569	MJ14	$3.8^{+0.4}_{-3.4}$	27.23 ± 0.24	$2.07^{+0.06}_{-0.08}$...
49.2	1161	64.040175	-24.079864	MJ14	27.46 ± 0.17	$3.45^{+0.04}_{-0.30}$...
49.3	...	64.026833	-24.069967	MJ14	$3.32^{+0.05}_{-0.39}$...
50.1	...	64.034790	-24.074585	MJ14	$2.38^{+0.10}_{-0.07}$...
50.2	...	64.039683	-24.078869	MJ14	28.33 ± 0.31	$3.54^{+0.05}_{-0.26}$...
50.3	...	64.026789	-24.069208	RK	28.31 ± 0.30	$3.09^{+0.00}_{-0.29}$...
51.1	1403	64.040160	-24.080290	MJ14	26.88 ± 0.11	...	Silver
51.2	958	64.033663	-24.074752	MJ14	24.63 ± 0.08	...	Silver
51.3	...	64.026620	-24.070494	MJ14	Silver
52.1	427	64.045857	-24.065830	MJ14	$3.9^{+0.5}_{-3.4}$	25.96 ± 0.07	$19.30^{+1.47}_{-4.09}$	Bronze
52.2	577	64.047698	-24.068668	MJ14	26.62 ± 0.12	$4.41^{+0.11}_{-0.50}$	Bronze
52.3	190	64.037724	-24.059826	MJ14	26.51 ± 0.11	$2.96^{+0.02}_{-0.12}$...
53.1	580	64.046023	-24.068800	MJ14	$3.0^{+0.2}_{-0.3}$	25.94 ± 0.08	$7.27^{+0.03}_{-0.48}$	Bronze
53.2	...	64.044776	-24.066682	MJ14	$8.73^{+0.20}_{-0.53}$...
53.3	223	64.036197	-24.060643	MJ14	26.68 ± 0.12	$2.76^{+0.08}_{-0.13}$	Bronze
54.1	712	64.046789	-24.071342	MJ14	$2.4^{+0.6}_{-0.2}$	26.39 ± 0.10	$2.94^{+0.01}_{-0.05}$	Bronze
54.2	464	64.041376	-24.064519	MJ14	$2.58^{+0.07}_{-0.14}$	Silver
54.3	276	64.037157	-24.062423	MJ14	26.25 ± 0.08	$4.38^{+0.15}_{-0.87}$	Silver
55.1	...	64.035233	-24.064726	MJ14	28.10 ± 0.22	$6.17^{+0.14}_{-0.15}$...
55.2	924	64.046070	-24.075174	MJ14	27.12 ± 0.13	$2.52^{+0.04}_{-0.06}$...
55.2a	...	64.046836	-24.075387	RK	$2.39^{+0.05}_{-0.03}$...
55.3	...	64.038514	-24.065965	MJ14	$2.42^{+0.05}_{-0.14}$...
56.1	...	64.035676	-24.083589	MJ14	29.11 ± 0.45
56.2	...	64.030097	-24.080924	MJ14
56.3	...	64.023847	-24.074998	MJ14
57.1	1027	64.026224	-24.076036	MJ14	26.02 ± 0.08	...	Bronze
57.2	...	64.028843	-24.079126	MJ14	Bronze
58.1	836	64.025187	-24.073582	MJ14	$3.3^{+0.3}_{-3.1}$	27.60 ± 0.17	$5.27^{+0.02}_{-0.35}$	Bronze
58.2	...	64.037730	-24.082390	MJ14	27.72 ± 0.18	$4.45^{+0.14}_{-0.36}$...
58.3	...	64.030481	-24.079220	MJ14	26.08 ± 0.13	$1.76^{+0.00}_{-0.13}$	Bronze
59.1	796	64.035851	-24.072799	MJ14	$2.1^{+0.2}_{-2.0}$	26.29 ± 0.07	$3.17^{+0.08}_{-0.10}$	Bronze
59.2	942	64.039936	-24.075622	MJ14	24.68 ± 0.04	$4.31^{+0.07}_{-0.06}$	Bronze
59.3	529	64.029105	-24.067658	MJ14	26.87 ± 0.11	$3.12^{+0.09}_{-0.04}$	Bronze
60.1	...	64.026724	-24.073720	MJ14	28.20 ± 0.24	$9.23^{+0.15}_{-1.67}$...
60.2	...	64.039708	-24.082514	MJ14	28.99 ± 0.40	$3.07^{+0.07}_{-0.09}$...
60.3	...	64.030984	-24.077181	MJ14	$2.86^{+0.45}_{-0.06}$...
61.1	...	64.026732	-24.073540	MJ14	28.18 ± 0.27	$9.20^{+0.11}_{-1.86}$...
61.2	...	64.039768	-24.082360	MJ14	$3.05^{+0.07}_{-0.09}$...
61.3	...	64.030593	-24.077760	MJ14	28.41 ± 0.41	$26.40^{+13.25}_{-17.44}$...

TABLE 2 — *Continued*

ID _{arc}	ID _{GLASS}	R.A. (deg.)	Dec. (deg.)	Cref.	$z_{\text{spec}}(1)$	$z_{\text{ref}}(1)$	$z_{\text{spec}}(2)$	$z_{\text{ref}}(2)$	z_{grism}	z_{Bayes}	F140W (mag.)	Magnification ¹	Sample
62.1	1135	64.026889	-24.079610	MJ14	24.70 ± 0.04	$1.54^{+0.01}_{-0.01}$	Bronze
62.2	1104	64.025993	-24.078892	MJ14	25.73 ± 0.06	$1.46^{+0.02}_{-0.00}$	Bronze
62.3	1370	64.036488	-24.084935	MJ14	27.78 ± 0.22	$1.25^{+0.01}_{-0.00}$...
63.1	1013	64.025535	-24.076650	MJ14	$4.0^{+0.5}_{-3.4}$	26.91 ± 0.12	$15.24^{+1.69}_{-1.95}$	Bronze
63.2	1143	64.028147	-24.079648	MJ14	$6.10^{+0.23}_{-0.66}$	Bronze
63.3	1350	64.037925	-24.084479	MJ14	28.17 ± 0.24	$2.98^{+0.39}_{-0.01}$	Bronze
64.1	1060	64.043100	-24.077590	MJ14	26.75 ± 0.11
64.2	500	64.031139	-24.067177	MJ14	26.11 ± 0.11
65.1	1091	64.042589	-24.075532	MJ14	26.30 ± 0.09	$1.58^{+0.02}_{-0.00}$	Bronze
65.2	380	64.028858	-24.064627	MJ14	26.61 ± 0.10	$1.48^{+0.01}_{-0.01}$	Bronze
65.3	...	64.037768	-24.071656	MJ14	$2.96^{+0.07}_{-0.03}$...
66.1	1262	64.038101	-24.082315	MJ14	$2.8^{+0.2}_{-0.3}$	27.46 ± 0.18	$4.00^{+0.08}_{-0.35}$...
66.2	898	64.026635	-24.074675	MJ14	27.05 ± 0.14	$7.01^{+0.15}_{-0.60}$...
67.1	1262	64.038075	-24.082404	MJ14	$2.9^{+0.8}_{-2.6}$	27.46 ± 0.18	$4.01^{+0.12}_{-0.32}$...
67.2	...	64.025451	-24.073651	MJ14	28.25 ± 0.25	$5.29^{+0.08}_{-0.35}$...
67.3	...	64.030363	-24.079019	MJ14	$1.89^{+0.04}_{-0.15}$...
68.1	817	64.036098	-24.073362	MJ14	$3.1^{+0.5}_{-2.7}$	25.82 ± 0.06	$2.79^{+0.10}_{-0.06}$	Bronze
68.2	...	64.040352	-24.076481	MJ14	23.06 ± 0.02	$3.78^{+0.05}_{-0.15}$	Bronze
68.3	503	64.028017	-24.067270	MJ14	26.46 ± 0.10	$3.26^{+0.02}_{-0.10}$...
69.1	...	64.036256	-24.074225	MJ14	Bronze
69.2	...	64.037681	-24.075260	MJ14	Bronze
69.3	...	64.028759	-24.069109	MJ14
70.1	...	64.038360	-24.072385	MJ14
70.2	...	64.038640	-24.072520	MJ14
70.3	...	64.032100	-24.065580	MJ14
71.1	...	64.027865	-24.077908	MJ14	28.68 ± 0.45
71.2	...	64.027410	-24.077382	MJ14
72.1	...	64.031937	-24.071316	MJ14	Bronze
72.2	...	64.030952	-24.070480	MJ14	28.33 ± 0.37
73.1	...	64.043712	-24.062603	MJ14	$1.5^{+1.0}_{-1.3}$	25.72 ± 0.09	$53.99^{+5.72}_{-18.97}$...
73.2	...	64.041861	-24.061243	MJ14	27.71 ± 0.26	$5.93^{+0.07}_{-0.28}$...
75.1	683	64.027940	-24.070843	JKP	$3.1^{+0.7}_{-2.8}$	27.48 ± 0.19	$5.26^{+0.07}_{-0.67}$...
75.2	...	64.040646	-24.080156	JKP	28.09 ± 0.27	$3.17^{+0.00}_{-0.25}$...
75.3	...	64.033095	-24.074110	JKP	$2.16^{+0.09}_{-0.05}$...
76.1	...	64.028127	-24.070769	JKP	28.92 ± 0.32	$5.43^{+0.00}_{-0.49}$...
76.2	...	64.040809	-24.080081	JKP	28.56 ± 0.42	$3.08^{+0.02}_{-0.26}$...
76.3	...	64.033054	-24.073948	JKP	$2.18^{+0.10}_{-0.05}$...
77.1	...	64.027688	-24.070863	JKP	$3.3^{+0.4}_{-3.1}$	27.48 ± 0.20	$4.92^{+0.08}_{-0.65}$...
77.2	...	64.040441	-24.080174	JKP	28.24 ± 0.30	$3.21^{+0.01}_{-0.25}$...
77.3	...	64.033187	-24.074305	JKP	$2.06^{+0.07}_{-0.06}$...
78.1	...	64.030426	-24.081586	JKP
78.2	...	64.034504	-24.083680	JKP
78.3	...	64.023305	-24.075333	JKP
79.1	...	64.042799	-24.066835	JKP
79.2	...	64.045584	-24.070439	JKP
79.3	...	64.033939	-24.061265	JKP
80.1	...	64.044641	-24.064573	JKP
80.2	...	64.046823	-24.067960	JKP
80.3	...	64.040052	-24.061000	JKP
81.1	...	64.043629	-24.067190	JKP
81.2	...	64.044861	-24.068615	JKP
200.1	...	64.028745	-24.080735	RK
200.2	...	64.023296	-24.075063	RK	29.38 ± 0.60
201.1	...	64.026265	-24.068700	RK	29.26 ± 0.51	$3.02^{+0.04}_{-0.23}$	Bronze
201.2	...	64.040054	-24.079110	RK	28.55 ± 0.35	$3.66^{+0.01}_{-0.35}$	Bronze
201.3	...	64.034916	-24.074576	RK	$2.25^{+0.07}_{-0.10}$	Bronze
202.1	...	64.030745	-24.070510	RK	Bronze
202.2	...	64.031721	-24.071343	RK	28.20 ± 0.24	...	Bronze
203.1	587	64.030729	-24.068882	RK	$2.5^{+0.5}_{-1.0}$	26.56 ± 0.09	$6.02^{+0.01}_{-0.53}$	Bronze
203.2	...	64.033525	-24.071381	RK	25.76 ± 0.08	$3.30^{+0.06}_{-0.13}$	Bronze
203.3	1063	64.042442	-24.077683	RK	26.84 ± 0.12	$2.55^{+0.03}_{-0.05}$...

TABLE 2 — *Continued*

ID _{arc}	ID _{GLASS}	R.A. (deg.)	Dec. (deg.)	Cref.	$z_{\text{spec}}(1)$	$z_{\text{ref}}(1)$	$z_{\text{spec}}(2)$	$z_{\text{ref}}(2)$	z_{grism}	z_{Bayes}	F140W (mag.)	Magnification ¹	Sample
204.1	...	64.037673	-24.061023	RK
204.2	...	64.042884	-24.063891	RK
204.3	...	64.048181	-24.070889	RK
205.1	...	64.038890	-24.060637	RK
205.2	...	64.043317	-24.062964	RK
205.3	...	64.049296	-24.071014	RK
206.1	...	64.043575	-24.059000	RK	$6.2^{+0.4}_{-5.0}$	27.32 ± 0.27	$10.94^{+0.68}_{-0.36}$...
206.2	264	64.047845	-24.062067	RK	26.57 ± 0.10	$19.40^{+4.22}_{-0.01}$...
206.3	...	64.050621	-24.065758	RK	$5.66^{+2.98}_{-0.15}$...
207.1	...	64.047137	-24.061139	RK	27.95 ± 0.16	$184.13^{+315.70}_{-98.63}$...
207.2	470	64.050867	-24.066531	RK	27.09 ± 0.18	$8.07^{+21.56}_{-0.68}$...
D22.1	...	64.034485	-24.066919	D15
D22.2	...	64.034181	-24.066489	D15
D22.3	...	64.034006	-24.066447	D15
D22.4	...	64.033953	-24.066906	D15
D27.1	...	64.041894	-24.077451	D15	28.03 ± 0.28
D27.2	...	64.036080	-24.073203	D15	27.30 ± 0.14
D30.1	...	64.040438	-24.075768	D15	26.62 ± 0.16
D30.2	...	64.035965	-24.072468	D15
D31.1	...	64.040482	-24.075471	D15	27.08 ± 0.14
D31.2	...	64.036057	-24.072411	D15	27.49 ± 0.20
D32.1	767	64.045119	-24.072336	D15	$3.4^{+0.1}_{-0.4}$	26.07 ± 0.07	$3.22^{+0.08}_{-0.01}$...
D32.2	...	64.040081	-24.066730	D15	25.12 ± 0.06	$1.56^{+0.06}_{-0.02}$...
D33.1	...	64.045367	-24.072519	D15	$3.4^{+0.2}_{-0.4}$	27.37 ± 0.17	$3.28^{+0.06}_{-0.03}$...
D33.2	...	64.039992	-24.066661	D15	25.12 ± 0.06	$1.62^{+0.07}_{-0.08}$...
D34.1	...	64.045499	-24.072674	D15	27.01 ± 0.13
D34.2	...	64.039916	-24.066609	D15
D36.1	...	64.035459	-24.067725	D15
D36.2	...	64.035603	-24.067953	D15
D36.3	...	64.035472	-24.068037	D15
D36.4	...	64.035183	-24.067917	D15

NOTE. — ID_{arc} for multiple image systems 19-22 are intentionally omitted for consistency with IDs from the recent literature (e.g. Jauzac et al. 2014). Entries where ID_{arc} ends in “p” refer to proposed multiple candidates which are less confident identifications. Entries where ID_{arc} ends in “a” offer alternative images to those with the same ID listed without “a.” Entries where ID_{GLASS} is listed as “...” had no match in the grism detection image. RA and DEC reference the HFF v1.0 60mas mosaics. Cref. lists the shortnames for publications in which the coordinates have appeared or will appear, if publication is in preparation. (MJ14 = Jauzac et al. (2014), TJ14 = Johnson et al. (2014), SR14 = Rodney et al. in prep., JPK = Kneib et al. in prep., D15 = Diego et al. (2015a), RK = Kawamata et al. (2015), JR14 = Richard et al. (2014), AZ13 = Zitrin et al. (2013), CG15 = Grillo et al. (2015), IB15 = Balestra et al. (2015)). Some multiple images have been targeted with spectroscopy by multiple authors. We list at most two references to spectroscopic redshifts, reporting the number of significant figures as they appear in each reference. (z_{grism}) is the grism redshift we measure in this work. The typical uncertainty on z_{grism} is 0.01, corresponding to a grism wavelength uncertainty of $\sim 50\text{\AA}$. z_{Bayes} is the redshift obtained for a multiple image system from hierarchical Bayesian modeling. z_{Bayes} (95% conf. limits) is only shown for systems with two or more reliable photometric redshift measurements. Objects for which F140W magnitudes (68% conf. limits) are listed as “...” are not detected in our photometric catalog. The magnification (68% conf. limits) was calculated using the best-fit lens model scaled to the spectroscopic redshift of the multiple image system, or z_{Bayes} if the spectroscopic redshift was not known. The “Sample” column refers to the category in which the HFF lens modeling assigned each multiple image based on the spectroscopic and photometric constraints. Only Gold and Silver images were used to constrain our lens model.

¹ Some multiple images have best-fit magnifications that are outside of the 68% confidence interval due to non-Gaussian errors.

² Systems 3 and 4 are believed to be different substructures of the same source galaxy due to the similar redshift and spatial position of the multiple images in each system.

³ The GLASS spectroscopic redshifts of 5.1 and 5.4 were determined after the HFF modeling procedure took place. Therefore, neither image was included in the Gold sample.

⁴ 12.3 does not belong to the Gold sample despite our measurement of $z_{\text{grism}} = 1.95$ because it is still not known whether 12.3 is the correct counter-image to 12.1 and 12.2, both of which lack spectroscopic confirmation.

⁵ The spectroscopic redshift of system 14 was reported erroneously by Jauzac et al. (2014) at $z = 2.0531$ using incomplete CLASH-VLT data. We measured $z_{\text{grism}} = 1.63$ for all three images in the system, in agreement with the redshift obtained using the complete CLASH-VLT data (Grillo et al. 2015, I. Balestra, private communication).

⁶ Balestra et al. (2015) published their spectroscopic redshifts after the HFF modeling teams graded the multiple images into the Gold, Silver and Bronze categories. We include them in this table for completeness and comparison with z_{grism} .

⁷ 29.1 was originally assigned as a Gold image from GLASS spectroscopy, but further analysis after the samples were chosen revealed that the spectroscopic confirmation was too tenuous. Therefore, this object should not be considered to be spectroscopically confirmed.

TABLE 3
GLASS SPECTROSCOPIC RESULTS FOR MULTIPLY AND SINGLY LENSED SOURCES

ID _{GLASS} ¹	ID _{arc}	R.A. (deg.)	Dec. (deg.)	F140W (mag.)	z_{phot} ²	z_{grism}	Quality	N_{lines} ³	Line(s)	Magnification
268	2.1	64.04116	-24.06185	23.01 ± 0.01	...	1.90	4	2	[O III] [O II]	8.26 ^{+0.97} _{-0.61}
248	2.2	64.04304	-24.06305	23.08 ± 0.01	2.4 ^{+0.1} _{-0.1}	1.89	4	2	[O II] [O III]	8.49 ^{+0.34} _{-0.70}
572	2.3	64.04748	-24.06885	22.97 ± 0.01	2.4 ^{+0.2} _{-0.3}	1.90	4	2	[O III] [O II]	4.13 ^{+0.29} _{-0.37}
494	3.1;4.1 ³	64.03080	-24.06720	23.32 ± 0.01	...	1.99	4	3	[O III] H β [O II]	4.13 ^{+0.03} _{-0.09}
372	3.2;4.2	64.03518	-24.07098	23.13 ± 0.01	2.5 ^{+0.1} _{-0.1}	1.99	4	2	[O III] H β	2.27 ^{+0.02} _{-0.06}
955	3.3;4.3	64.04185	-24.07581	23.21 ± 0.01	...	1.99	4	3	[O III] H β [O II]	3.20 ^{+0.12} _{-0.01}
519	5.1	64.03245	-24.06848	21.58 ± 0.00	...	2.09	4	2	[O III] H β	14.37 ^{+0.24} _{-1.09}
520	5.2	64.03264	-24.06866	23.78 ± 0.01	2.4 ^{+0.1} _{-0.1}	2.09	4	2	[O III] H β	25.51 ^{+1.78} _{-1.25}
584	5.3	64.03355	-24.06947	23.14 ± 0.01	1.8 ^{+0.6} _{-0.4}	2.10	4	2	[O III] H β	4.47 ^{+0.08} _{-0.00}
1031	5.4	64.04355	-24.07696	25.56 ± 0.05	2.5 ^{+0.1} _{-0.2}	2.09	4	2	[O III] H β	2.55 ^{+0.00} _{-0.03}
312	7.1	64.03981	-24.06310	24.89 ± 0.04	2.3 ^{+0.2} _{-0.3}	2.09	4	2	[O III] [O II]	401.21 ^{+130.09} _{-310.13}
321	7.2	64.04058	-24.06354	24.95 ± 0.03	...	2.09	4	1	[O III]	14.51 ^{+0.36} _{-2.02}
1033	10.1	64.02602	-24.07717	23.96 ± 0.02	...	2.29	3	1	[O III]	8.47 ^{+0.11} _{-0.73}
456	12.3 ⁴	64.02898	-24.06665	22.24 ± 0.01	1.9 ^{+0.1} _{-0.1}	1.96	4	0	...	2.84 ^{+0.11} _{-0.00}
889	14.1	64.02623	-24.07433	22.97 ± 0.01	...	1.63	4	3	[O III] H β [O II]	4.58 ^{+0.09} _{-0.29}
880	14.2	64.03104	-24.07896	22.92 ± 0.01	...	1.63	4	2	[O III] [O II]	2.16 ^{+0.15} _{-0.05}
1213	14.3	64.03583	-24.08132	22.74 ± 0.01	1.7 ^{+0.2} _{-0.3}	1.63	4	3	[O III] H β [O II]	4.78 ^{+0.05} _{-0.29}
957	15.1	64.02687	-24.07574	26.16 ± 0.07	2.8 ^{+0.1} _{-0.2}	2.34	3	1	[O III]	15.01 ^{+0.43} _{-2.52}
1186	16.1	64.02406	-24.08090	...	2.2 ^{+0.1} _{-1.6}	1.96	4	3	[O III] H β [O II]	5.23 ^{+0.16} _{-0.10}
1362	16.3	64.03160	-24.08577	23.65 ± 0.01	...	1.97	4	1	[O III]	6.05 ^{+0.30} _{-0.27}
1197	17.3	64.02335	-24.08158	2.23	4	2	[O III] [O II]	4.27 ^{+0.05} _{-0.04}
750	23.1	64.04454	-24.07208	24.22 ± 0.02	2.4 ^{+0.1} _{-0.2}	2.09	4	2	[O III] [O II]	3.06 ^{+0.03} _{-0.03}
332	23.3	64.03432	-24.06372	24.40 ± 0.02	2.3 ^{+0.1} _{-0.2}	2.09	4	3	[O III] H β [O II]	4.09 ^{+0.03} _{-0.08}
209	26.1	64.04646	-24.06040	26.70 ± 0.15	3.3 ^{+0.2} _{-0.2}	2.19	3	2	[O III] [O II]	14.66 ^{+0.30} _{-3.24}
347	27.2	64.04746	-24.06601	23.49 ± 0.02	...	2.11	4	1	[O III]	69.69 ^{+17.58} _{-2.07}
394	28.1;28.2 ⁵	64.03667	-24.06732	20.91 ± 0.00	0.8 ^{+0.1} _{-0.1}	0.94	4	0	...	65.86 ^{+57.83} _{-11.08}
753	29.3	64.04462	-24.07148	24.56 ± 0.03	2.4 ^{+0.1} _{-0.2}	2.28	4	1	[O III]	3.40 ^{+0.04} _{-0.05}
141	...	64.03330	-24.05824	24.94 ± 0.03	0.8 ^{+0.1} _{-0.1}	0.82	4	2	H α [O III]	1.59 ^{+0.01} _{-0.01}
98	...	64.02949	-24.05639	25.68 ± 0.05	2.6 ^{+0.2} _{-0.2}	2.14	4	3	[O III] H β [O II]	2.26 ^{+0.01} _{-0.07}
94	...	64.03309	-24.05633	22.23 ± 0.01	1.2 ^{+0.3} _{-0.1}	1.36	4	3	H α [O III] [O II]	1.91 ^{+0.00} _{-0.03}
90000	...	64.02515	-24.05637	21.70 ± 0.01	0.3 ^{+0.2} _{-0.1}	0.39	4	0
108	...	64.03986	-24.05719	24.80 ± 0.03	2.5 ^{+0.1} _{-0.1}	2.22	4	3	[O III] H β [O II]	2.51 ^{+0.03} _{-0.01}
90001	...	64.05564	-24.06030	...	0.4 ^{+0.1} _{-0.2}	0.41	4	0
155	...	64.02725	-24.05911	21.73 ± 0.00	0.3 ^{+0.2} _{-0.1}	0.37	4	0
451	...	64.05742	-24.06632	25.47 ± 0.04	1.3 ^{+0.2} _{-0.2}	1.35	4	4	H α [S II] [O III] [O II]	2.54 ^{+0.01} _{-0.05}
90002	...	64.05920	-24.06649	17.97 ± 0.00	0.3 ^{+0.1} _{-0.1}	0.31	4	1	H α	...
186	...	64.04089	-24.06035	20.02 ± 0.00	0.4 ^{+0.1} _{-0.1}	0.40	4	0

NOTE. — GLASS spectroscopic results for all multiply-lensed and the first 10 singly-lensed galaxies. The full catalog is given in the electronic edition. z_{phot} lists the best-fit and 68% confidence limits on the photometric redshift from the ASTRODEEP photometric catalog. z_{grism} is the grism spectroscopic redshift we measure in this work. The nominal uncertainty on z_{grism} is ~ 0.01 for objects with $N_{\text{lines}} \geq 1$. However, the redshift uncertainty is more variable for objects with $N_{\text{lines}} = 0$, which were confirmed by fitting the continuum grism spectra to SED templates (G. Brammer, in prep.). The full GLASS redshift PDFs are available online⁸.

¹ Objects with ID_{GLASS} in the format 9XXXX come from an extraction based on a different alignment than the one used to extract the other GLASS IDs.

² The images for which z_{phot} is not shown are either contaminated or not detected in the photometric catalog.

³ Systems 3 and 4 are believed to be different substructures of the same source galaxy due to the similar redshift and spatial position of the multiple images in each system.

⁴ The uncertainty in z_{grism} for ID_{arc} = 12.3 is ~ 0.02 , rather than the nominal ~ 0.01 because the redshift was obtained by fitting its continuum emission in the grism to SED templates rather than through the identification of emission lines.

⁵ 28.1 and 28.2 were detected as the same object in the segmentation map used to extract the grism data. Like 12.3, the redshifts of 28.1 and 28.2 were obtained by fitting the continuum emission in the grism to SED templates.